

Nonadiabatic kinetics in the intermediate coupling regime: comparing molecular dynamics to an energy grained master equation

Darya Shchepanovska¹, Robin J. Shannon¹, Basile F. E. Curchod^{2,*}, and David R. Glowacki^{1,3,4,*}

¹School of Chemistry, University of Bristol, Bristol, BS8 1TS, UK; ²Department of Chemistry, Durham University, Durham, DH1 3LE, UK; ³Intangible Realities Laboratory, University of Bristol, BS8 1UB, UK;

⁴Department of Computer Science, University of Bristol, BS8 1UB, UK

[*glowacki@bristol.ac.uk](mailto:glowacki@bristol.ac.uk); basile.f.curchod@durham.ac.uk

Abstract

Here we outline and test an extension of the energy grained master equation (EGME) for treating nonadiabatic (NA) hopping between different potential energy surfaces, which enables us to model the competition between stepwise collisional relaxation and kinetic processes which transfer population between different potential energy surfaces of the same spin symmetry. By incorporating Zhu-Nakamura theory into the EGME, we are able to treat nonadiabatic passages beyond the simple Landau-Zener approximation, along with corresponding treatments of zero-point energy and tunnelling probability. To evaluate this NA-EGME approach, we carried out detailed studies of the UV photodynamics of the volatile organic compound C₆-hydroperoxyaldehyde (C₆-HPALD) using on-the-fly ab initio molecular dynamics and trajectory surface hopping. For this multi-chromophore molecule, we show that the EGME is able to quantitatively capture important aspects of the dynamics, including kinetic timescales, and diabatic trapping. Such an approach provides a promising and efficient strategy for treating the long-time dynamics of photo-excited molecules in regimes which are difficult to capture using atomistic on-the-fly molecular dynamics.

1. Introduction

The accuracy of molecular photodynamic simulations in the excited state is inherently constrained by the dimensionality of the system. Exact non-relativistic quantum mechanical dynamics of a wavepacket can be described by solving the time-dependent Schrödinger equation, but exponential scaling limits this approach to small molecular systems. At the opposite end of the scale, there is a growing interest in describing the nonadiabatic dynamics of very large systems characterised by exciton transfer between chromophores.¹ In fact, an analytical description of nonadiabatic transitions for a simple one-dimensional two-state system in the weak coupling limit has been available since 1932, developed simultaneously, and separately, by Landau, Zener, and Stueckelberg.² In many cases Landau-Zener (LZ) theory works reasonably well even for larger, multidimensional systems. Later, Zhu and Nakamura built on this framework to produce a set of exact nonadiabatic transition probabilities for different types of nonadiabatic curve crossings.³ Zhu-Nakamura (ZN) theory is valid over the entire coupling regime, is fully analytical, and incorporates tunnelling contributions. Like LZ theory, it is formulated in a single dimension.

On-the-fly trajectory-based semiclassical dynamics accounts for the full dimensionality of a molecular system. For example, Tully's fewest switches surface hopping (FSSH) is a well-known and efficient way of simulating femtosecond timescale processes in the excited state,⁴ where the time evolution of a wavepacket is approximated by a swarm of independent trajectories that classically propagate the nuclear degrees of freedom on a potential energy surface (PES) calculated on-the-fly.

Each trajectory can stochastically switch between electronic states in regions of strong coupling. While FSSH has known shortcomings (including overcoherence, and neglect of tunnelling and interference effects⁵), it often provides an accurate and scalable method that is now widely used to explore photodynamic phenomena, also for atmospheric chemistry.⁶ Given that FSSH typically has a sub-femtosecond integration time step, pushing the simulation into the nanosecond regime necessitates compromises with respect to the electronic structure method and number of trajectories. It has been suggested that this bottleneck might be overcome through machine learned energies and couplings.⁷

For longer timescale simulations in the statistical regime, alternatives to conventional nonadiabatic dynamics strategies are needed. The energy grained master equation (EGME) is the numerical implementation of the exact master equation which discretises the density of states ρ , recasting it in matrix form. The EGME has recently been applied to the study of non-RRKM reaction kinetics in the gas phase,⁸ in solution,⁹ and in surface chemistry.¹⁰ Unlike FSSH, where an electronic structure calculation is performed at each step of a trajectory, an EGME calculation needs only the energies, frequencies and rotational constants of the relevant stationary points. This allows for the use of more computationally demanding electronic structure calculations and detailed sensitivity analyses on the results. The EGME also enables treatment of collisional activation and dissipation from the system. Furthermore, unlike molecular dynamics simulations where zero-point energy can leak, vibrational zero-point energy at the stationary points can be included explicitly in an ME calculation. Approaches to zero-point energy conservation in quantum-classical trajectories exist,¹¹ but they are not adopted in the standard fewest switches surface hopping (FSSH) algorithm used in this work. Tunnelling corrections may also be included in the framework of the EGME approach using an asymmetric Eckart barrier¹² or semiclassical WKB theory.¹³ Solving the ME returns temperature and pressure dependent species profiles, making it a useful tool for modelling atmospheric or interstellar reactions.

Nonadiabatic analogues of standard statistical rate theories generalise classical transition state theory (TST) to reactions involving multiple PESs.¹⁴ For example, intersystem crossings have been successfully modelled by using both the LZ and ZN expression for the inter-state surface hopping probability at the minimum energy crossing point (MECP).¹⁵ Until recently, simulation of intersystem crossings in the surface hopping framework has been limited by the need for the global calculation of the spin-orbit coupling matrix elements¹⁶ or spin-orbit coupling gradients.¹⁷ It is now possible to run semiclassical trajectory surface hopping simulations that include coupling between states of arbitrary multiplicity.¹⁸ Using the LZ approach to describe coupling between states with differing multiplicity works well in the weak coupling regime, but fails for strong coupling.^{2a} A nonadiabatic EGME model (NA-EGME) of internal conversion should instead use the ZN expression, which is able to accurately treat the analytical nonadiabatic transition probabilities for the full range of energies and couplings,^{3b} giving the LZ result in the weak coupling limit, and the transition state theory result in the strong coupling limit. The ZN description of the coupling region can also be formulated to include contributions from tunnelling through the crossing barrier. In contrast to the full-DOF description of quantum-classical dynamics, the ZN equations are only formulated for 1-D crossings. Herein, we provide evidence that – for seam-like crossings – the ZN approach offers a good approximation to describing nonadiabatic transitions between adiabatic states.

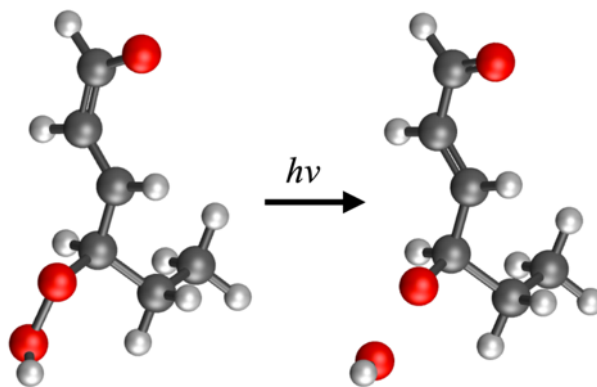


Figure 1: Main reaction channel for C₆-HPALD photodissociation in 300-400 nm range.¹⁹

In this work we apply the NA-EGME to predict the dissociation rate of a photoexcited bi-chromophoric hydroperoxy aldehyde, C₆-HPALD, whose primary photodissociation channel is shown in figure 1. In order to evaluate the validity of this approach, we show that the NA-EGME results are similar to the outcomes of a FSSH molecular dynamics simulations. HPALDs represent a class of molecules important in atmospheric chemistry, and it has been suggested that they participate in OH radical recycling at low NO_x regions of the troposphere.²⁰ As a product of isoprene oxidation, they contain an α,β -enone chromophore which absorbs sunlight in the UV range, which is in close proximity to a labile peroxide bond. Previous experiments investigating the photodissociation kinetics of C₆-HPALD reported OH radical production under UV light.¹⁹ In this paper, we are less concerned with the atmospheric details of HPALD photodissociation, but rather with C₆-HPALD as a prototypical example of a multi-chromophore system with an interesting seam-like nonadiabatic coupling topology between two low-lying excited states. We show that the dissociation rate obtained using a NA-EGME model is in agreement with the results of nonadiabatic FSSH dynamics, at a significantly reduced computational cost.

This paper will be structured as follows. Firstly, we describe how nonadiabatic effects can be included in an EGME model using ZN transition probabilities. Second, we describe the electronic structure calculations used to characterise the relevant excited states of C₆-HPALD in the Franck-Condon region, and along the dissociative coordinate. Third, we describe the FSSH and NA-EGME calculations and their adiabatic counterparts. Fourth, we compare the results of these contrasting methods for a single isolated reaction coordinate which corresponds to the wavepacket moving over a transition state on the S₁ surface leading to photodissociation. Lastly, we extend both models to include all rotational conformers of C₆-HPALD.

2. Methods

2.1 Constructing a nonadiabatic master equation

The energy grained master equation (EGME) is a Markov-state model that has found widespread application to non-equilibrium problems in chemical kinetics.^{9,21} Most applications of EGME models focus on reactive processes on a single electronic state and do not incorporate nonadiabatic coupling. While strategies for calculating microcanonical rate coefficients for nonadiabatic processes do exist, to our knowledge there has only been one attempt to incorporate such transitions into an EGME framework: specifically, Plane *et al.*^{21b} modelled temperature and pressure dependent intersystem crossing kinetics by treating the extended seam between the singlet and triplet state as a dividing surface. The minimum energy crossing point (MECP) between the states was treated as a pseudo-transition state, and the probability of spin-forbidden hopping transitions between these states was

calculated by convoluting the density of states at the MECP with the LZ expressions to obtain microcanonical rate coefficients.

Building on the work of Plane *et al.*, we have extended the NA-EGME to calculate the rate of HPALD photodissociation, where the nonadiabatic transition of interest involves coupling between two states of the same multiplicity – i.e., significantly stronger coupling than the intersystem crossing investigated by Plane *et al.* The LZ model is ill-suited to internal conversion as it assumes the inter-state coupling is localised, and weak. For these reasons, we used ZN theory to describe nonadiabatic transition probabilities in the coupling region. The ZN equations produce the correct analytical hopping probability coefficients over the full range of coupling regimes, for a 1-D nonadiabatic tunnelling type crossing,^{3b, 22} returning the LZ result in the limit of weak coupling, and the classical transition state theory result in the limit of strong coupling.

An adiabatic master equation model (A-EGME, illustrated in figure 2) is constructed from any number of connected potential energy wells (isomers) and the transition states between them. In order to make the problem computationally tractable, the energy of each species is discretised into bins or grains of a set size. The population density across each energy grain of every isomer in the system is then defined by a vector $\mathbf{n}(E,t)$, and it is possible to formulate a set of coupled differential equations in terms of $\mathbf{n}(E,t)$ that describe the time-evolution of the grain populations. Recasting these differential equations in matrix form defines the chemical master equation.

$$\frac{\partial \mathbf{n}(E,t)}{\partial t} = \mathbf{M}\mathbf{n}(E,t) \quad (1)$$

The matrix \mathbf{M} is expressed as $[\omega(\mathbf{P}-\mathbf{I})-k]$, where ω is the Lennard Jones collision frequency, \mathbf{P} is a matrix of transition probabilities between grains, \mathbf{I} is the identity, and k is a diagonal matrix of energy-resolved microcanonical rate constants, $k(E)$, for the reactive process. In the EGME, population transfer between grains can arise due to interactions with a bath or through reactive loss/gain to a connected isomer. Energy transfer as a result of bath interactions is typically modelled using an exponential down model. For reactions between different isomers, population transfer can only occur between corresponding grains of the same energy. This is included in the model through unimolecular microcanonical rate coefficients $k(E)$ calculated from Rice-Ramsperger-Kassel-Marcus (RRKM) theory. The RRKM microcanonical rate coefficient at energy E is

$$k(E) = \frac{W(E)}{h\rho(E)} \quad (2)$$

where $W(E)$ is the sum of rovibrational states at the optimised transition state geometry, and $\rho(E)$ is the density of rovibrational states at the isomer.

Because the EGME can be used to model out-of-equilibrium phenomena,²³ it is often applied to reactions in atmospheric and combustion chemistry which cannot be modelled with equilibrium TST techniques due to the non-Boltzmann distribution of energy in isomers. This allows us to replicate the non-equilibrium energy distribution of a wavepacket directly following photoexcitation.

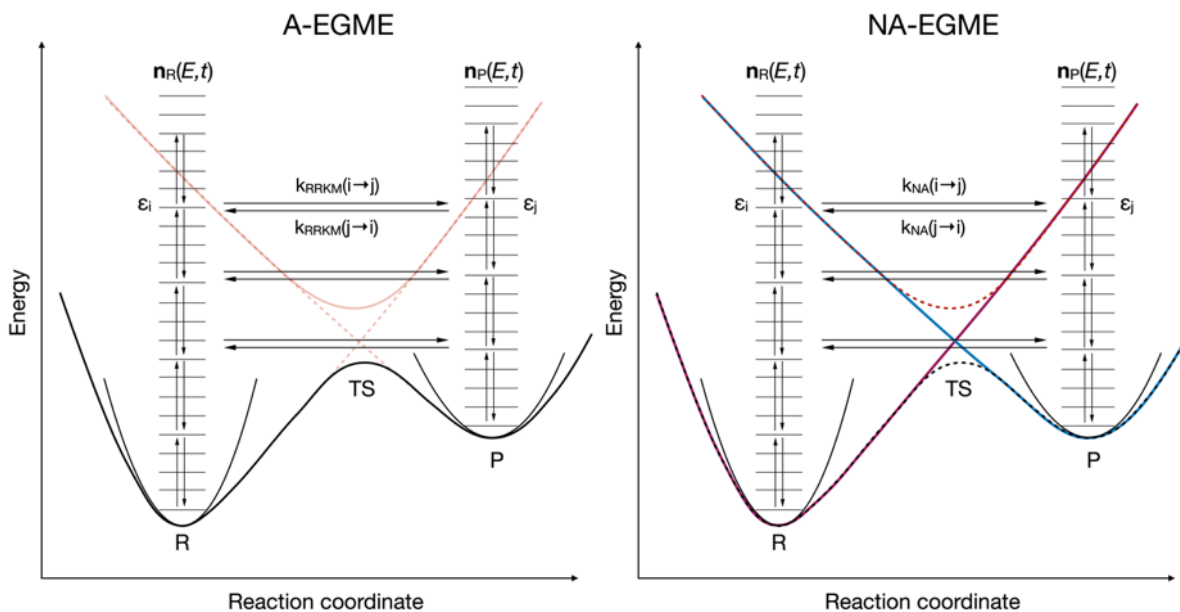


Figure 2: Left hand panel shows a standard A-EGME model describing a reactant and product species connected by a transition state. Right hand panel shows the NA-EGME, with nonadiabatic transitions integrated through the inclusion of energy resolved ZN transition probabilities to the upper state.

The NA-EGME model, illustrated in figure 2, is constructed analogously to the conventional ground state A-EGME, except that the microcanonical rate coefficients are not calculated through RRKM theory. Nonadiabatic coupling between states is included through an energy resolved ZN expression for the transition probabilities P_{ZN} between two diabatic states in the vicinity of a crossing point. We can then compute a set of nonadiabatic microcanonical rate coefficients $k_{NA}(E)$ which transfer population between the different diabatic states. The expression for $k_{NA}(E)$ is similar to the RRKM expression in equation 2,

$$k_{NA}(E) = \frac{N_{TS}(E)}{h\rho_{S_1}(E)} \quad (3)$$

where the density of states at the optimised S_1 minimum is ρ_{S_1} and N_{TS} is the convolution of the ZN transition probabilities P_{ZN} and density of states at the transition state ρ_{TS} .

$$N_{TS}(E) = \int_0^E \rho_{TS}(E - E')P_{ZN}(E)dE' \quad (4)$$

The complete equations for P_{ZN} are available in the SI, and implemented in MESMER (master equation solver for multi-well energy reactions).²⁴

3. Computational details

3.1 Characterising the excited state PESs

C_6 -HPALD is a conformationally flexible molecule. A systemic rotor search performed in Avogadro V1.2.0 finds 7 conformational isomers which we label A-G. Ground state geometries of these

conformers were then optimised with DFT/PBE0/TZVP and their analytical frequencies confirm that these geometries are local minima on the ground state PES.

Excited state properties, including energies, nuclear gradients, and nonadiabatic couplings, can be calculated accurately and efficiently with linear response time dependent density functional theory (LR-TDDFT). LR-TDDFT, like DFT, is formally exact on the condition that the true frequency-dependent exchange correlation functional is used. Its shortfalls are well documented, including its tendency to underestimate energies of states with high charge transfer character²⁵ or regions of the PES with strong coupling between ground and excited states.²⁶ Nevertheless, LR-TDDFT is widely used for nonadiabatic dynamics simulations of larger systems due to its favourable scaling with basis set size.²⁷ Employing LR-TDDFT for excited state dynamics, however, always benefits from a careful validation of its accuracy in comparison to high-level wavefunction methods.

To determine a method for running FSSH in the relevant region of the PES, we performed a number of excited state benchmarks at the S_0 geometry of the lowest energy conformer (B) of C₆-HPALD. A scan along the PES cross section of the -O-OH internal coordinate was initiated at the S_0 geometry of conformer B to validate the use of LR-TDDFT/PBE0/6-31G (calculated for 5 singlets) against MS(4)-CASPT2(10,8)/6-31G* and a number of other methods. The active space of the MS-CASPT2 calculation was selected to include the bonding and anti-bonding orbitals of the peroxide and α,β -enone chromophores, as well as the lone pairs on the oxygen atoms. All DFT/LR-TDDFT calculations in this paper were performed in Gaussian 16.²⁸ Ground state energies at the optimised geometries were refined with density fitted CCSD(T)-f12//cc-pVDZ-f12//def2-QZVPP in Molpro 2019.²⁹ MS-CASPT2 calculations were performed in OpenMolcas v18.09.³⁰

The transition state (S_1 -TS) on the S_1 surface was optimised using an eigenvector following Bery algorithm in Gaussian 16²⁸ with LR-TDDFT/PBE0/6-31G. Finding this first order saddle point on the S_1 surface was not a trivial task: because the seam is quite sharp, optimisation steps that were too large would cause it to fall down the steep slopes of the ridge. The S_1 -TS geometry was verified through a vibrational frequency analysis that yielded a single imaginary frequency. An intrinsic reaction coordinate (IRC) scan was performed, initiated at this S_1 -TS geometry. Geometries of each conformer were optimised in the S_1 state with the optimisation starting at their respective S_0 geometry. The minimum energy conical intersection (MECI) between the S_1 and S_2 states was optimised by using the search algorithm described by Harvey *et al.*³¹

3.2 Predicting the photoabsorption cross section to calculate photolysis rate

The photoabsorption cross section of C₆-HPALD has yet to be measured experimentally. We can predict it *ab initio* by using the nuclear ensemble approach based on a harmonic Wigner distribution in the ground state³² which captures the broadening of the spectral bands. Ground state frequencies used to generate the Wigner distribution were calculated for each conformer with DFT/PBE0/TZVP. For each of the 7 conformers, 100 nuclear configurations are sampled from their respective distribution. We calculate the absorption in the 300-400 nm range into the S_1 and S_2 electronic states separately, as well as the combined spectrum. For each sample point the vertical transitions and oscillator strengths are calculated with LR-TDDFT/PBE0/TZVP. Each peak is overlaid with a Lorentzian curve whose phenomenological broadening is set to 0.05 eV to return a continuous spectrum. The final photoabsorption cross section is a linear combination of the spectra for each conformer where the Boltzmann weights of the conformers ω_{conf} are calculated from their CCSD(T) electronic energies. We approximated the Gibbs free energy by the electronic energy because free energy corrections (from PBE0/TZVP frequencies) did not change the ordering of states.

3.3 Trajectory surface hopping dynamics

All trajectory dynamics simulations were performed using the following protocol, unless stated otherwise. Fewest switches surface hopping (FSSH) simulations were performed in Newton-X.^{14b, 33} Energies and gradients of the first four singlet states (S_0 - S_3) were calculated at each step with LR-TDDFT/PBE0/6-31G using Gaussian 09.³⁴ Energy based decoherence corrections were applied, as described by Granucci and Persico,³⁵ with the decoherence parameter α set to 0.1 a.u. Nonadiabatic coupling terms between electronic states were calculated using a time-derivative coupling scheme.³⁶

The importance of the nonadiabatic effects was quantified by comparing against ab initio molecular dynamics (AIMD) in which the nonadiabatic coupling between states was set to 0, effectively restricting the trajectories to the S_1 state. AIMD calculations were also performed in Newton-X with identical initial conditions to the FSSH run.

Starting geometries and velocities for the trajectories were generated by randomly sampling points from a ground state Wigner distribution. For each conformer this distribution was constructed using DFT/PBE0/TZVP level normal mode frequencies at the optimised S_0 geometries, where a larger basis set is selected to improve the quality of the distribution. In total, we ran 250 FSSH and 50 AIMD trajectories, whose initial conditions corresponded to the Wigner distribution of conformer C. A further 109 trajectories were performed with both FSSH and AIMD, corresponding to the realistic conformer distribution where the number of trajectories corresponds to the Boltzmann weight of the conformer in the ground state. All trajectories were initiated on the S_1 electronic state as it corresponded to the strongest peak in the actinic region, $\lambda > 320$ nm, of the absorption cross section (available in the SI).

All trajectories were propagated up to 4 ps or until photodissociation was observed. Total energy was conserved in all trajectories up to the end point of the trajectory. Because LR-TDDFT fails to describe homolytic bond dissociation, a dissociative outcome causes a failure in energy conservation, signalling trajectory termination. Classical nuclei were propagated with a 0.5 fs time step.

3.4 Constructing a nonadiabatic EGME model from stationary points on the excited state PES

Each electronic structure calculation used to construct an EGME model was performed at the same level of theory (LR-TDDFT/PBE0/6-31G) as that used for surface hopping dynamics so that we might directly compare the results. Energies of all stationary points were specified with respect to the energy of the geometry optimised S_1 minimum which was treated as the reactant well in the model. Zero-point energy corrections were not used when defining the relative energies so as to make a direct comparison with results of dynamics calculations, in which ZPE was not rigorously constrained.

The electronic structure theory codes which we utilized provided states energies in the adiabatic (S_0 , S_1 , S_2 , etc.) representation. However, as illustrated in Figure 2, the NA-EGME treats the different states in the diabatic representation (in this case an $n\pi^*$ and $n'\sigma^*$ state), and requires as input an analytical form of the diabatic states in the vicinity of the crossing point to determine P_{ZN} at the seam. To derive a diabatic representation from the adiabatic energies, we considered only the coordinate along the imaginary eigenvector of the S_1 -TS Hessian, investigating 1D motion along the 3N-7 dimensional coupling seam. The eigenvector describing this motion takes the system across the $n\pi^*/n'\sigma^*$ seam, which corresponds to extension of the peroxide bond and loss of OH, denoted by reaction coordinate R . Energies of the S_1 and S_2 adiabatic states across this coordinate are used to fit the diabatic states near the TS. We do this by constructing a simple Hamiltonian, $\mathbf{H}(R)$, which includes the two diabatic states and a coupling between them (H_{12}), assumed to be constant in that region.

$$\mathbf{H}(R) = \begin{pmatrix} H_{11}(R) & H_{12} \\ H_{12} & H_{22}(R) \end{pmatrix} \quad (6)$$

Analytical expressions for its two eigenvalues, λ_1 and λ_2 are determined by diagonalizing $\mathbf{H}(R)$. These eigenvalues correspond to the S_1 and S_2 adiabatic states respectively. Calculated adiabatic states were fitted to the analytical forms of the diabats given in equation 7. We assumed the dissociative state $H_{22}(R)$ to have the form of an exponential decay, and the bound state, $H_{11}(R)$, to have the form of a harmonic well.

$$\begin{aligned} H_{11}(R) &= A_{\pi^*}(R - \beta_{\pi^*})^2 + \varepsilon_{\pi^*} \\ H_{22}(R) &= A_{\sigma^*} \exp(-R\beta_{\sigma^*}) + \varepsilon_{\sigma^*} \end{aligned} \quad (7)$$

The fitted parameters (available in the SI) were used in the NA-EGME calculation to determine P_{ZN} and calculate a set of microcanonical rate constants for each energy grain.

The initial population vector $\mathbf{n}(E, t_0)$ was set up with N energy grains. To replicate the energy distribution of the wavepacket at the start of the dynamics, $\mathbf{n}(E, t_0)$ must mirror the initial conditions used in the FSSH calculations. Each initial condition sampled from the Wigner ensemble corresponds to an initial energy, a sum of its kinetic energy and its potential energy referenced to S_1 . The distribution of total energies resembles a normal distribution, with an average initial energy above the S_1 minimum. This average energy corresponds to the n_i^{th} energy grain in the population vector $\mathbf{n}(E, t)$ so the EGME calculations are initiated with 100% of the initial population in this grain.

We used a grain size of 50 cm^{-1} in all EGME calculations and standard temperature and pressure (300K and 760 Torr) to replicate atmospheric conditions. Collision parameters used for the bath gas, He, were $\varepsilon = 10.2 \text{ K}$ and $\sigma = 2.55 \text{ \AA}$ and the collisional energy transfer was treated using an exponential down model.³⁷ The collisional energy transfer parameter is set to 250 cm^{-1} , a value which is typical under standard atmospheric conditions.^{21c} Photodissociation was assumed to be irreversible and the dissociation products were treated as a sink. To quantify the impact of nonadiabatic effects at the $n\pi^*/n'\sigma^*$ seam in these EGME calculations, the same model was re-run without allowing nonadiabatic transitions, using a standard non-equilibrium ground state EGME model. Microcanonical $k(E)$ were calculated using RRKM theory.

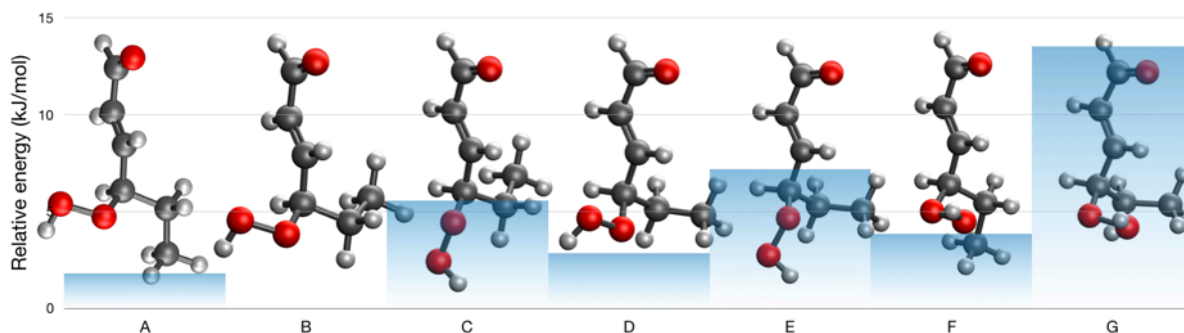


Figure 3: Geometries of the 7 rotational isomers of C_6 -HPALD. Relative energies, shown on chart, are refined with df-CCSD(T)-f12//cc-pVDZ-f12//def2-QZVPP.

The NA-EGME model was then modified by substituting MS(4)-CASPT2/6-31G* energies at the same LR-TDDFT optimised stationary points to refine the EGME result. These calculations use the same frequencies and rotational constants calculated with LR-TDDFT/PBE0/6-31G. Single point energy calculations were performed for the following geometries: the S_1 minimum of the B

conformer; geometries found by taking steps along the imaginary eigenvector of S_1 -TS. For the latter case, a crossing point between the diabatic surfaces is found at a small displacement from the S_1 -TS geometry. New diabats were fitted to the results of the scan, leading to slightly different ZN parameters.

All EGME calculations reported in this study were performed using the open source master equation solver, MESMER.^{24, 38}

4. Results and Discussion

4.1 Characterising the S_1 and S_2 PESs in the Franck-Condon region and at the crossing seam

Ground state geometries and relative CCSD(T) energies of all 7 conformers are shown in Figure 3. Optimising these rotamer structures on the S_1 PES with LR-TDDFT converged on 7 distinct structures that maintain the orientation of the peroxide and (-CH₂CH₃) branches such that there are multiple S_1 minima. Conformer B remained the lowest energy conformer on the S_1 PES.

Our predicted photoabsorption cross section $\sigma(\lambda)$, available in the SI, indicated that the majority of the photoexcitation in the UV-Vis region is into the S_1 state. Integrating over $\sigma(\lambda)$, actinic flux, and quantum yield in the actinic region we can make an ab-initio estimate of the photolysis rate. Assuming a unity quantum yield we predict it to be $1.4 \times 10^{-4} \text{ s}^{-1}$, within a factor of three of the observed experimental rate of $6.3 \pm 0.1 \times 10^{-5} \text{ s}^{-1}$.¹⁹ The cross section indicates that in the actinic region the strongest peak corresponds to absorption into the S_1 state.

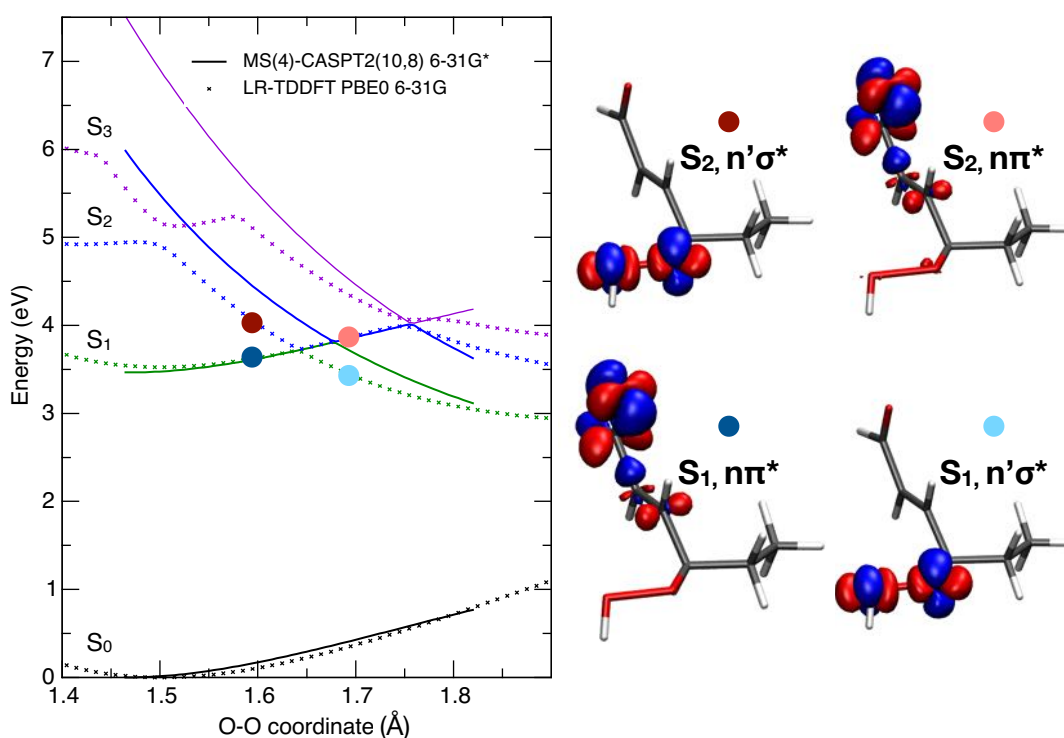


Figure 4: Energies of the first 4 excited states calculated with LR-TDDFT/PBE0/6-31G and MS(4)-CASPT2(10,8)/6-31G*, alongside electron density difference plots between S_0 and specified state at 2 points along the peroxide bond coordinate illustrating the change in diabatic character.

Shapes of the excited state potentials along the peroxide bond coordinate calculated with LR-TDDFT/PBE0/6-31G and MS-CASPT2(10,8)/6-31G* show good qualitative agreement. On this basis, we decided to use LR-TDDFT/PBE0/6-31G as the electronic structure method for all FSSH and AIMD calculations in this paper. Rigid scans along the peroxide bond dissociation coordinate in Figure 4 show a near degenerate region between the S_1 and S_2 states at 1.65 Å, and between S_2 and S_3 states at 1.76 Å. Benchmarks using larger basis sets show that as the bond extends beyond 1.75 Å, LR-TDDFT provides a poor description of homolytic dissociation. This, however, will not be a significant problem for the dynamics because the S_1 potential is dissociative beyond this point, at which point trajectories were terminated.

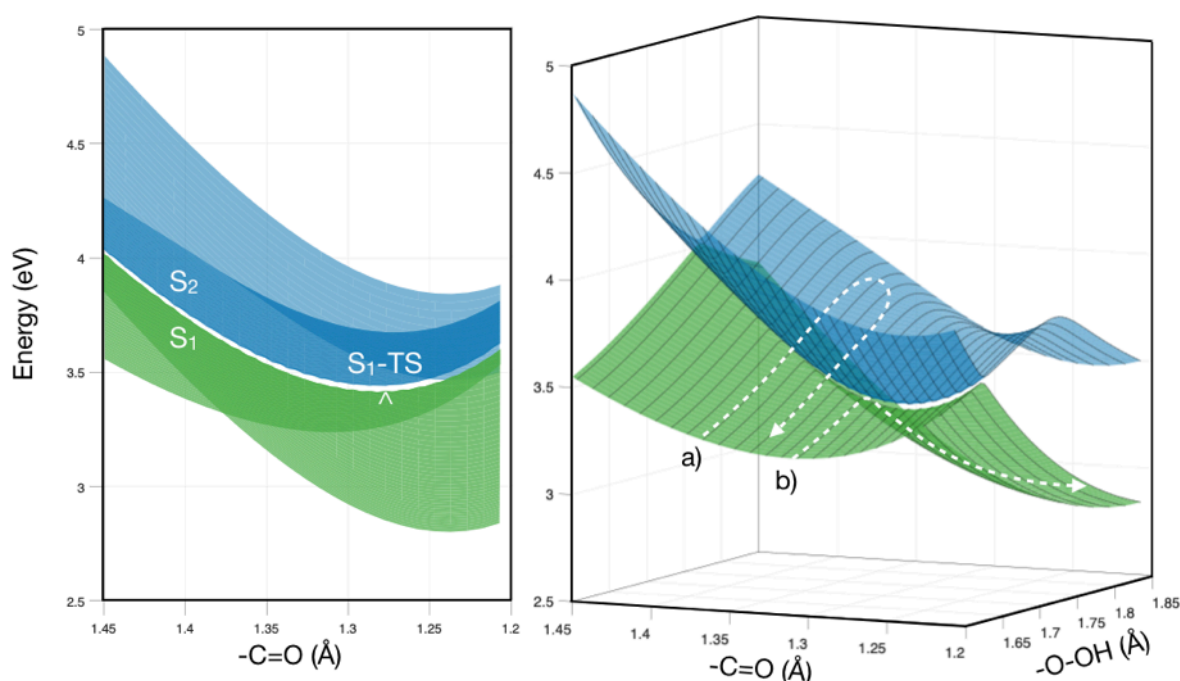


Figure 5: Scan of the S_1/S_2 nonadiabatic seam initiated at S_1 -TS, excitation energies calculated with LR-TDDFT/PBE0/6-31G. Left panel highlights the extended near-degenerate (3N-7) seam. a) Diabatic trapping mechanism; b) Adiabatic passage across seam leading to loss of OH.

In the density difference plots shown in figure 4, it's visible that the $n\pi^*$ transition which characterises the S_1 state in the bound region of the PES (O-O extended to 1.6 Å) is located mostly on the α,β -enone chromophore. At the same geometry, the $n'\sigma^*$ transition to the S_2 state is located mostly along the -O-OH bond. When the peroxide bond is extended to 1.7 Å the ordering of the diabatic states swaps, such that the S_1 state is characterised by the $n'\sigma^*$ transition. The region of strong nonadiabatic coupling observed between the S_1 and S_2 at 1.65 Å in Figure 4 is a single point on an extended (3N-7) seam where the $n\pi^*$ and $n'\sigma^*$ diabatic states cross. We located critical points along this seam which included an S_1/S_2 MECI as well as a saddle point on the S_1 surface (S_1 -TS) which is the minimum energy geometry in the space of this seam. The energy of the MECI is 31.3 kJ mol⁻¹ above the S_1 minimum of the lowest energy conformer, B. The energy of the S_1 -TS is at 16.1 kJ mol⁻¹ relative to conformer B. Visualising the normal mode corresponding to the only imaginary frequency at the S_1 -TS showed synchronization between stretching in the -O-OH coordinate and compression in the C=O coordinate. This highlights that this mode couples the α,β -enone and peroxide chromophores and therefore will be important for describing the reaction coordinate. Furthermore, the remarkably high value of the imaginary frequency ($\nu_{\text{im}} = -3534.1 \text{ cm}^{-1}$) illustrates the sharpness of the (3N-7) seam in

the vicinity of the S_1 -TS. To visualise this seam we performed a rigid 2D scan along the $-C=O$ and $-O-OH$ stretching coordinates of C_6 -HPALD that correspond to the two coupling chromophores. Results of this scan are shown in Figure 5.

An intrinsic reaction coordinate (IRC) scan initiated at the S_1 -TS geometry converges on the dissociated structure and the S_1 minimum of conformer C, as can be seen in Figure 6. Energies, frequencies, and rotational constants at these critical points are tabulated in the SI.

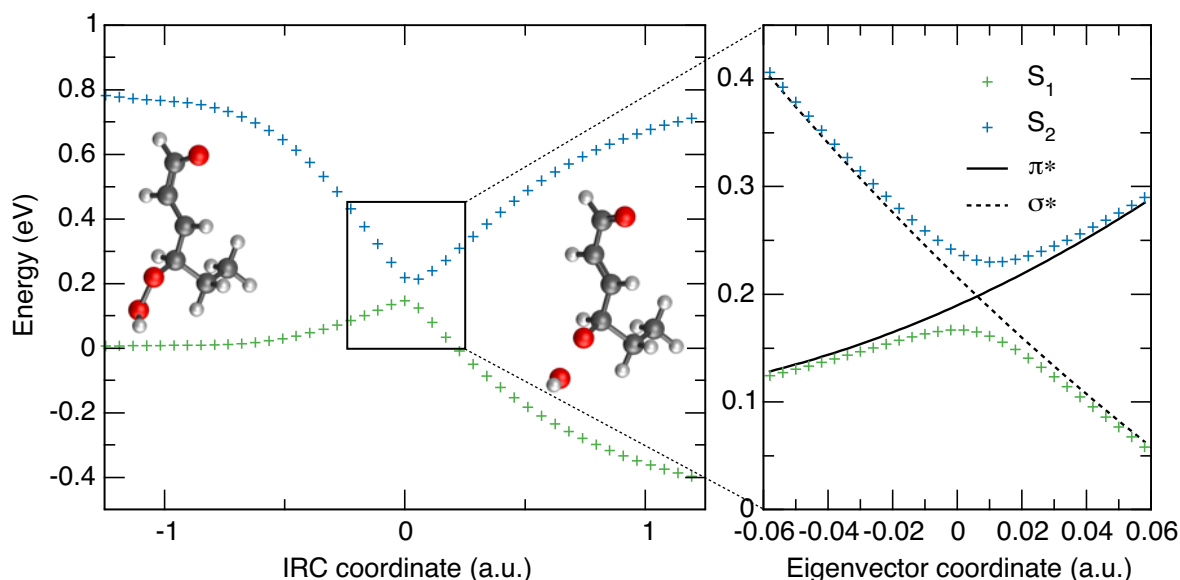


Figure 6: Intrinsic reaction coordinate scan started at the S_1 -TS. Energy is shown relative to the S_1 minimum of conformer C. Geometries are shown at the terminal step of the IRC scan. Right panel shows a scan across the TS geometry along the eigenvector of the imaginary normal mode. Fitted diabatic states used in the NA-EGME calculation are shown in black.

4.2 Direct comparison between NA-EGME and FSSH for a single conformer

Our exploration of the excited state PES located a direct reaction coordinate between the S_1 minimum of conformer C and the S_1 -TS, shown by the IRC in Figure 6. In the following section, we consider a simple photodissociation model based on a potential well (S_1 -C) and a single barrier (S_1 -TS) linked by this reaction coordinate, that ignores all other C_6 -HPALD conformations.

4.2.1 Description of the seam crossing and OH loss rate from FSSH dynamics

We began by running 50 AIMD and FSSH trajectories, whose initial conditions were sampled from the ground state Wigner distribution of conformer C. The two sets of trajectories shown in Figure 7 are projected on to the $-C=O$ and $-O-OH$ coordinates, illustrating the passage of trajectories across the seam. By observing HPALD dynamics prior to dissociation we see that the molecule remains in the S_1 potential well for a number of vibrational periods and explores the available phase space within its initial conformation.

For all 50 FSSH trajectories the net adiabatic population remained largely on the S_1 state, with 90% hopping to the S_2 state at some point during the run. Only a single trajectory hopped to the S_3 state, and no population on S_0 was ever observed. On this timescale we expect that the dynamics are limited to the S_1 and S_2 adiabatic states. In the Franck-Condon region of the PES the S_1 state exhibits $n\pi^*$ character and is near an S_1 PES minimum. AIMD trajectories in Figure 7 indicate that for loss of OH

to occur, the -O-OH coordinate must extend in concert with the compression of the -C=O bond, causing the S_1 state to change character from predominantly $\pi\pi^*$ to the dissociative $n'\sigma^*$ character. The wavepacket must necessarily proceed across the seam adiabatically, however hopping to the non-dissociative S_2 state can occur.

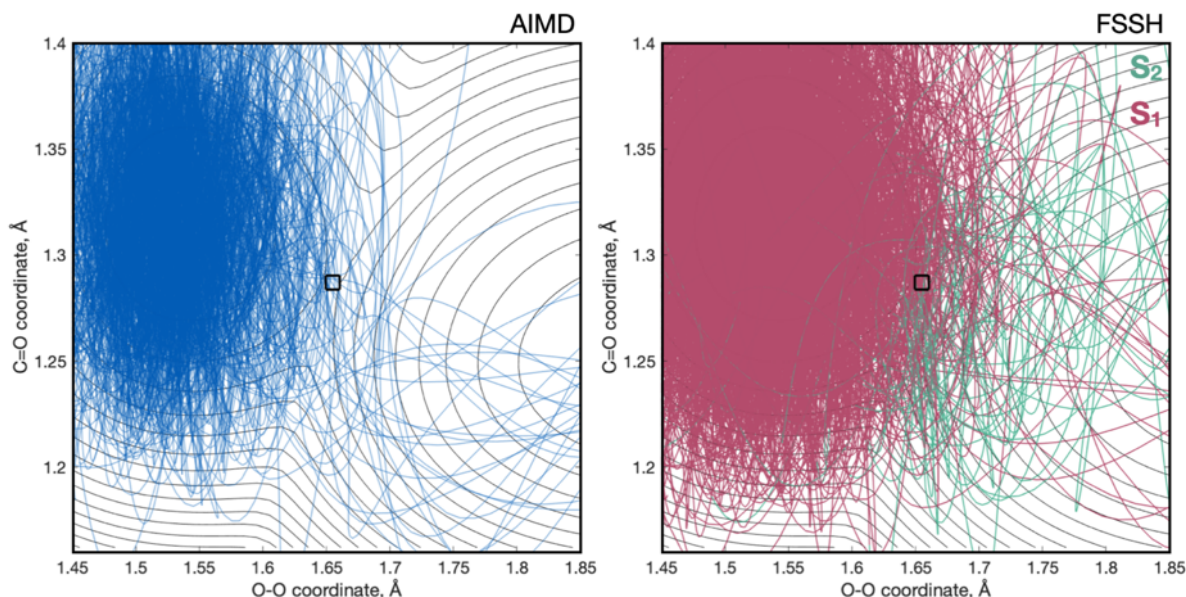


Figure 7: Projection of 50 AIMD and FSSH trajectories of conformer C into the -C=O and -O-OH coordinates. FSSH panel (right) illustrates the switch from S_1 to S_2 with a colour change. Background contour plot shows the shape of the S_1 PES from a rigid scan initiated at the S_1 -TS (indicated by the black square) then scanned across these two coordinates, illustrating the S_1 potential energy well where the trajectories are initialised, and the dissociative potential on the other side of the barrier.

In Figure 7, we observe that while many FSSH trajectories that travel across the barrier rebound back towards the S_1 well, almost all AIMD trajectories which cross the barrier dissociate. In the nonadiabatic case such motion visibly corresponds with a switch to the S_2 state. This mechanism is referred to as diabatic trapping (originally described by Martínez *et al.* as up-funnelling) whereby a trajectory remains on the same diabatic state as it crosses the coupling region thereby preserving its electronic character.³⁹ Because of this, OH loss is faster for AIMD trajectories since crossing this (3N-7) seam will necessarily lead to a dissociative outcome, whereas in FSSH the trajectory might become trapped in S_2 and rebound instead. A similar upwards hopping process is observed in the work of Blancafort *et al.* in the bis-adamantyl radical cation that contains two weakly coupled chromophores.⁴⁰ We note some similarities between their system and ours, such as the extended near-degenerate seam between two adiabatic states. Qualitatively, we note that diabatic trapping is likely in systems where the CI branching space vectors are of significantly different magnitude, as is the case here (CI branching space vectors available in the SI).

Next, we consider the rate of dissociation as determined by the dynamics. Three possible outcomes have been observed in the FSSH results: loss of OH (38 trajectories), loss of HO_2 (9 trajectories), and no dissociative reaction (3 trajectories). The corresponding AIMD results are as follows: loss of OH (45 trajectories), loss of HO_2 (3 trajectories), and no dissociative reaction (2 trajectories). A dissociative outcome is defined as the extension of either the C-OOH or O-OH bond coordinate beyond 1.75 Å and 1.9 Å respectively. Benchmark scans of the PES along these coordinates have shown a potential barrier at 1.65 Å, beyond which the molecule is unlikely to recombine. Dissociating trajectories terminated soon after this nonadiabatic barrier is crossed due to the unreliability of LR-TDDFT in its description of homolytic dissociation. These trajectories are included in the analysis up

to the point of dissociation since we can assume that once the bond has extended beyond the threshold, the rate coefficient for reassociation is very small. Loss of HO₂ is a minor dissociative channel which has been suggested experimentally for other peroxides.⁴¹ Its mechanism in C₆-HPALD appears to be linked with diabatic trapping because all FSSH trajectories terminating in this way show an S₂ to S₁ hop 20 fs prior to dissociation. Given its low probability, and because it cannot be treated with a kinetic model, the HO₂ loss channel is excluded in the following analyses.

To ensure that the FSSH result is converged we ran another 200 trajectories by using the same 50 initial conditions but inserting a new random seed for the surface hopping algorithm 4 times. In Figure 8 we see that the results are well converged with as few as 50 trajectories. Biexponential fits of HPALD population decay are available in the SI. A biexponential least-squares fit indicates that there are two separate decay timescales.⁴² The fast decay corresponds to trajectories that dissociated ballistically (OH loss takes less than 200 fs), while others remained in the pre-dissociative S₁ well until the trajectory was able to cross the seam allowing more time for intra-vibrational relaxation to occur. Decay constants for the slow fraction of the decay are 1.87 ps for FSSH and 1.29 ps for AIMD.

4.2.2 Calculating rate of OH loss using an NA-EGME model

Our NA-EGME model assumes that to describe the primary photodissociation channel leading to the loss of OH we need only to consider the $n\pi^*/n'\sigma^*$ state coupling along a 1-D coordinate over the top of the TS. This necessitated only a normal mode analysis at the S₁ minimum of conformer C (S₁-C) and the S₁-TS barrier which is energetically 14.13 kJ mol⁻¹ higher. The optimised MECI is 15.2 kJ mol⁻¹ above the S₁-TS. The 3N-7 dimensional geometry of the nonadiabatic seam means the MECI is unlikely to be an important critical point since the wavepacket does not need to pass through it to reach the S₂ state. For this reason, the MECI's influence on the dissociation rate can be neglected and we choose not to include it in the model. Total energies of the 50 initial conditions are normally distributed with the average initial energy at 453.4 kJ mol⁻¹ above the S₁-C minimum. This energy corresponds to the 758th grain in the population vector $\mathbf{n}(E,t)$ and so, the EGME calculations were initiated with 100% of the population in this energy grain.

The HPALD decay rates calculated using A-EGME and NA-EGME are presented in Figure 8, illustrating that the photolysis rates obtained with the trajectory-based approaches are quantitatively similar to those obtained from EGME models. Including nonadiabatic effects slows down the decay rate approximately 6-fold ($\tau_{\text{NA-EGME}} = 2.72$ ps) in comparison to the rate calculated when nonadiabaticity is neglected ($\tau_{\text{A-EGME}} = 0.45$ ps). The decay rate is shown to be robust to the initial energy grain distribution and small variations in frequencies by the sensitivity analyses provided in the SI.

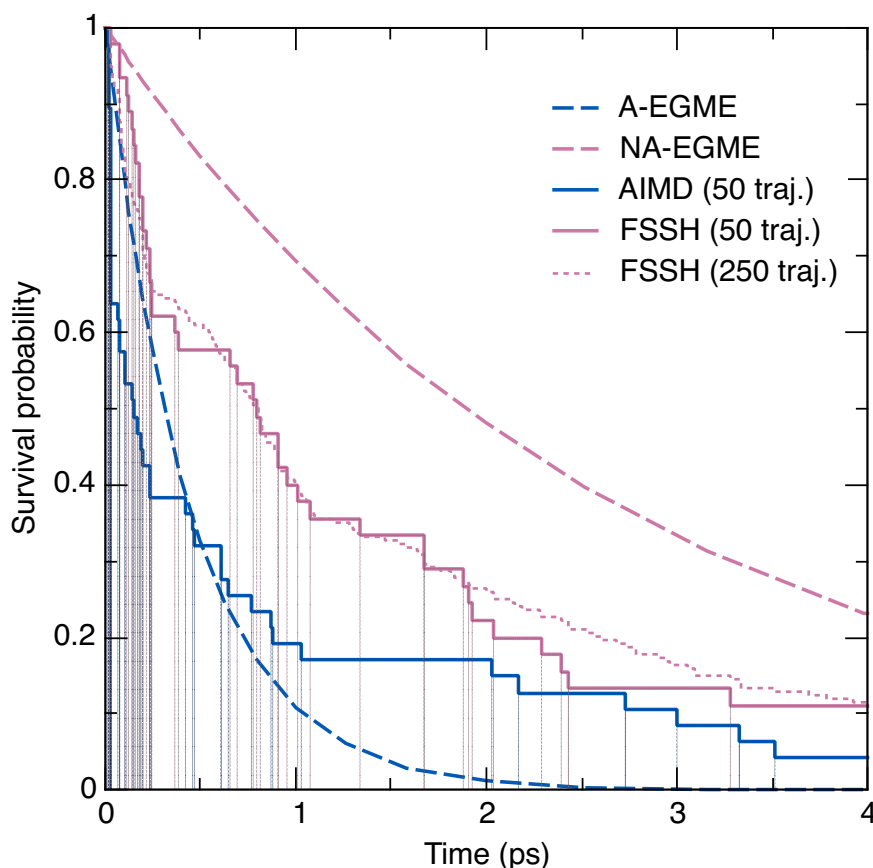


Figure 8: Comparison of C_6 -HPALD decay rate between EGME and trajectory-based methods for conformer C. Convergence of FSSH at 50 trajectories indicated by the similarity to the 250-trajectory result.

4.3 Comparison of the two extended models, including all conformers

Having established that treating the photodissociation of conformer C in isolation shows good agreement between NA-EGME and FSSH results we can extend this simple model to include all conformers of C_6 -HPALD shown in Figure 3. For the dynamics calculations we simply projected the ground state conformer distribution into the excited state such that the set of trajectory initial conditions was representative of the rotamer distribution. Boltzmann weights of the A-G conformers (listed in the SI) determine the number of trajectories to be run for each. For TST-type methods like EGME, molecular torsions can be challenging because the rigid rotor approximation breaks down due to the highly anharmonic hindered rotor modes. Ideally, each conformation and its corresponding TS should be treated separately.⁴³ However, for 7 rotational conformers this approach would necessitate a cumbersome search for 30 separate TSs in a $3N$ dimensional phase space. Instead, we propose a pared down model that uses the global conformer minimum (S_1 -B) and the S_1 -TS to calculate the OH loss rate.

4.3.1 Conformational changes and realistic dynamics of OH loss in FSSH trajectories

The relative numbers of trajectories initiated at each conformer corresponds to their Boltzmann weight in the ground state calculated using CCSD(T) energies: A: 24; B: 50; C: 5; D: 16; E: 3; and F: 11.

Dihedral angles ϕ_1 and ϕ_2 can be used as a shorthand to distinguish the conformers over the course of a trajectory. This can be seen in Figure 9 which shows all of the dissociating trajectories exploring the rotational phase space and highlighting that the timescale of conformer interconversion is comparable to that of OH loss. Trajectories corresponding to conformers C and F especially tend to remain conformationally locked, supporting our previous assumption that conformer C could be treated independently. There is a flux of trajectories from conformer B to C suggesting that the rotational barrier between them is small.

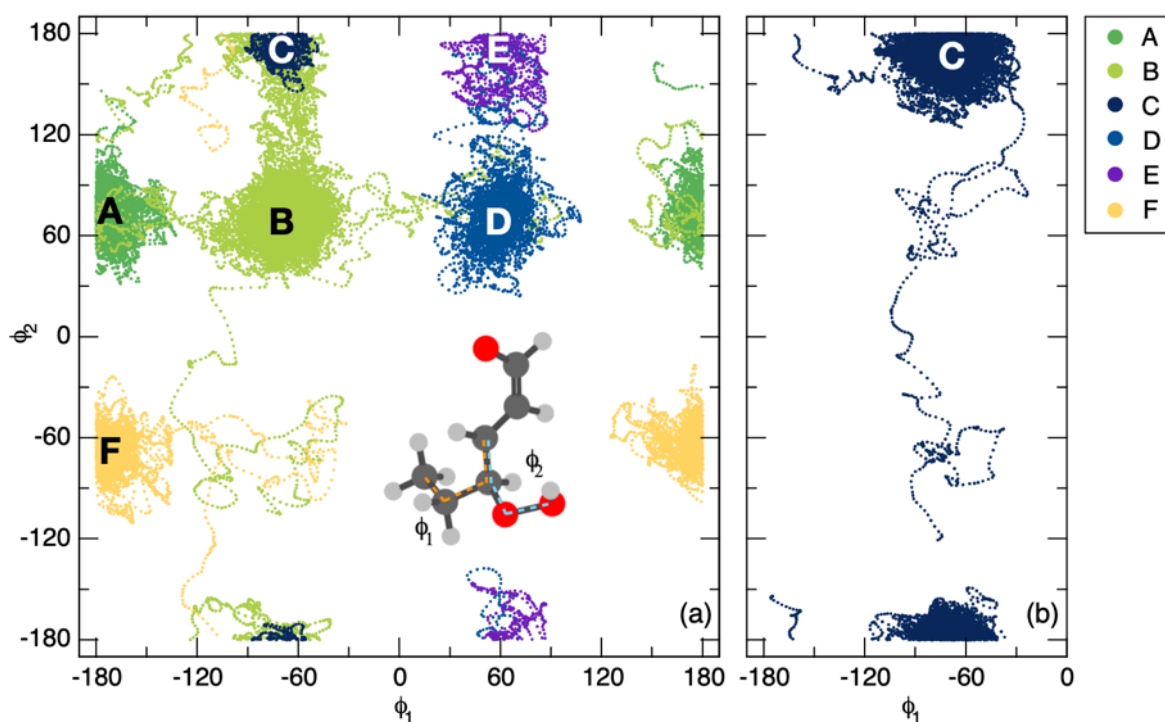


Figure 9: HPALD conformer interconversion over a 4 ps timescale. Left panel shows the evolution of the two dihedral angle coordinates ϕ_1 and ϕ_2 that define the conformation of the HPALD molecule at a given time step for all 109 FSSH trajectories. Right panel shows 50 trajectories of conformer C only.

Of the 109 FSSH trajectories initiated on the S_1 state we observed the following outcomes: loss of OH (50 trajectories), loss of HO_2 (15); no dissociation (43). The corresponding results of the AIMD simulations are: loss of OH (82), loss of HO_2 (10), no dissociation (17). The 95% margin of error shown by the error bars in Figure 10c illustrates that the difference between dissociative outcomes in adiabatic vs. nonadiabatic simulations is significant.

Analysis of the mean adiabatic population shows that on average population remained on the S_1 surface, rarely falling below 95%, with a fraction of population moving into the S_2 state. Very few trajectories hopped into the S_3 state and no population of the S_0 state was observed on the timescale of the simulation. The survival probability is fitted to an exponential decay, with a first order lifetime, τ_{FSSH} , of 4.6 ps. AIMD dynamics of OH loss are better fitted to a double exponential, shown in Figure 10d. Approximately a quarter of trajectories are dissociated on a fast timescale with a lifetime, τ_{fast} , of 58 fs. The rest of the trajectories dissociate on a similar timescale to the FSSH simulations with lifetime, τ_{slow} , of 2.4 ps.

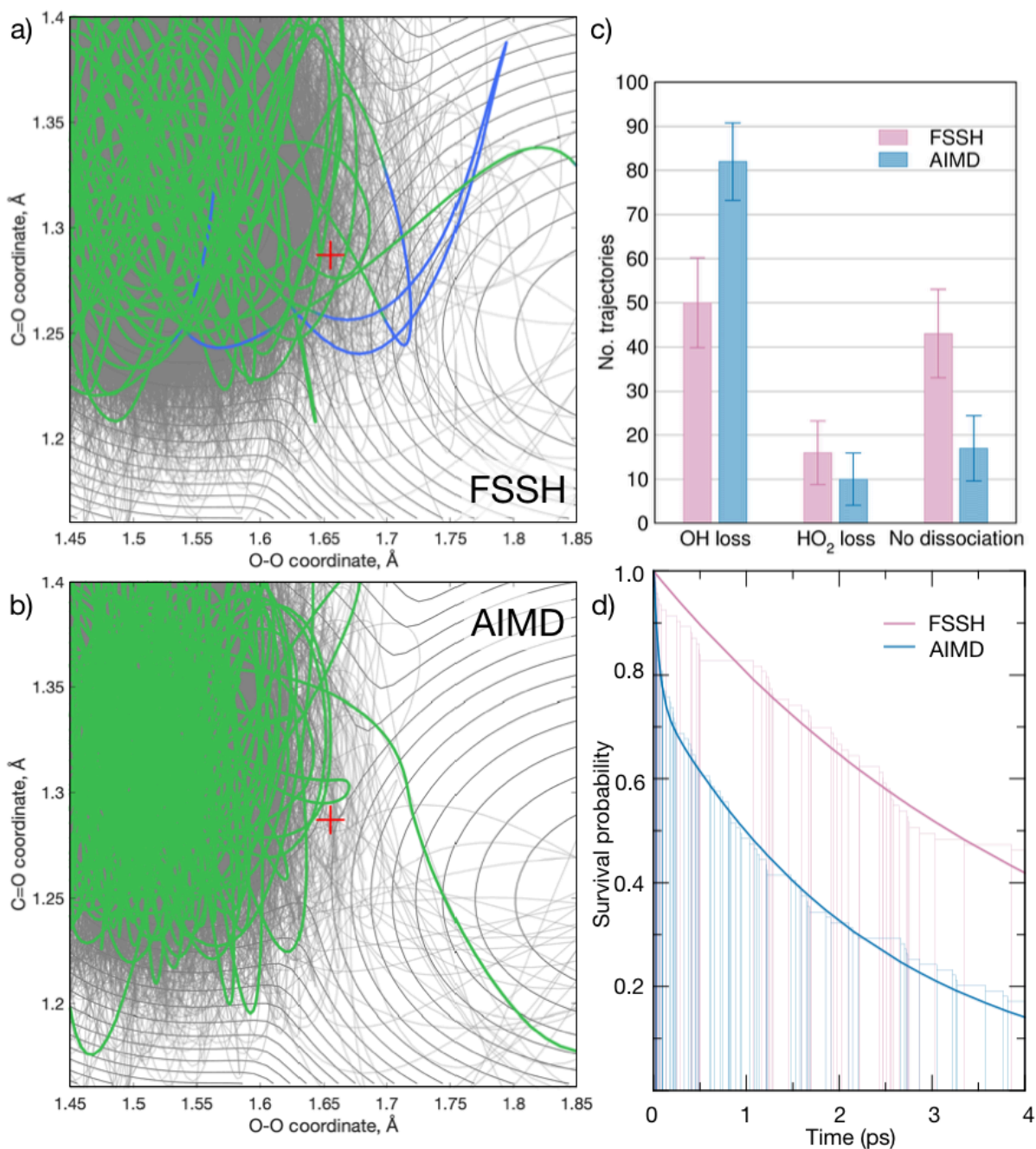


Figure 10: Dynamics results for all conformers of C₆-HPALD. a) An example of a diabatically trapped trajectory where the switch to S₂ is illustrated by a colour change. b) Example AIMD trajectory that moves in the S₁ well for a number of vibrational periods before crossing the barrier and dissociating immediately. c) Outcomes of the 109 trajectories with 95% confidence intervals showing that differences between FSSH and AIMD are significant. d) Survival probabilities with respect to OH loss, fitted to exponential decay functions.

4.3.2 An approximate all-conformer NA-EGME model for OH loss

Now that we have the results of trajectory dynamics initiated from a realistic ground state conformer distribution we construct a new, more realistic, NA-EGME model. Since a large fraction (50 out of 109) of the trajectories were initiated from the conformer B initial condition we use its S₁ minimum as the reactant well (S₁-B) and the S₁-TS. The average initial energy of these trajectories was at 487.0 kJ mol⁻¹ above the S₁-B minimum corresponding to the 814th energy grain in the population vector

$n(E,t)$. Results of the NA-EGME calculations based on this model are shown in Figure 11. We see that including nonadiabaticity once again has a strong effect on the microcanonical rate coefficients shown in the inset. The nonadiabatic lifetime τ_{ZN} is 1.7 ps, once again $\sim 6\times$ greater than the adiabatic lifetime, $\tau_{\text{RRKM}} = 0.3$ ps.

We have tested the importance of torsional anharmonicity using the hindered rotor approach, as implemented in MESMER. This sensitivity analysis ensures that the presence of anharmonic rotational modes does not significantly alter the ratio of densities of states, and the corresponding decay constants. Normal mode frequencies corresponding to torsional motion were projected out of the Hessian.⁴⁴ Results of rigid torsional scans performed over 4 torsional bonds at the S_1 -B minimum and S_1 -TS geometries were input into the MESMER calculation. Results available in the SI show that incorporating these torsional effects does not significantly impact the reaction profiles. We suggest this could be due to the similarity between torsional profiles at the S_1 minimum and TS geometries that result in a cancellation of errors.

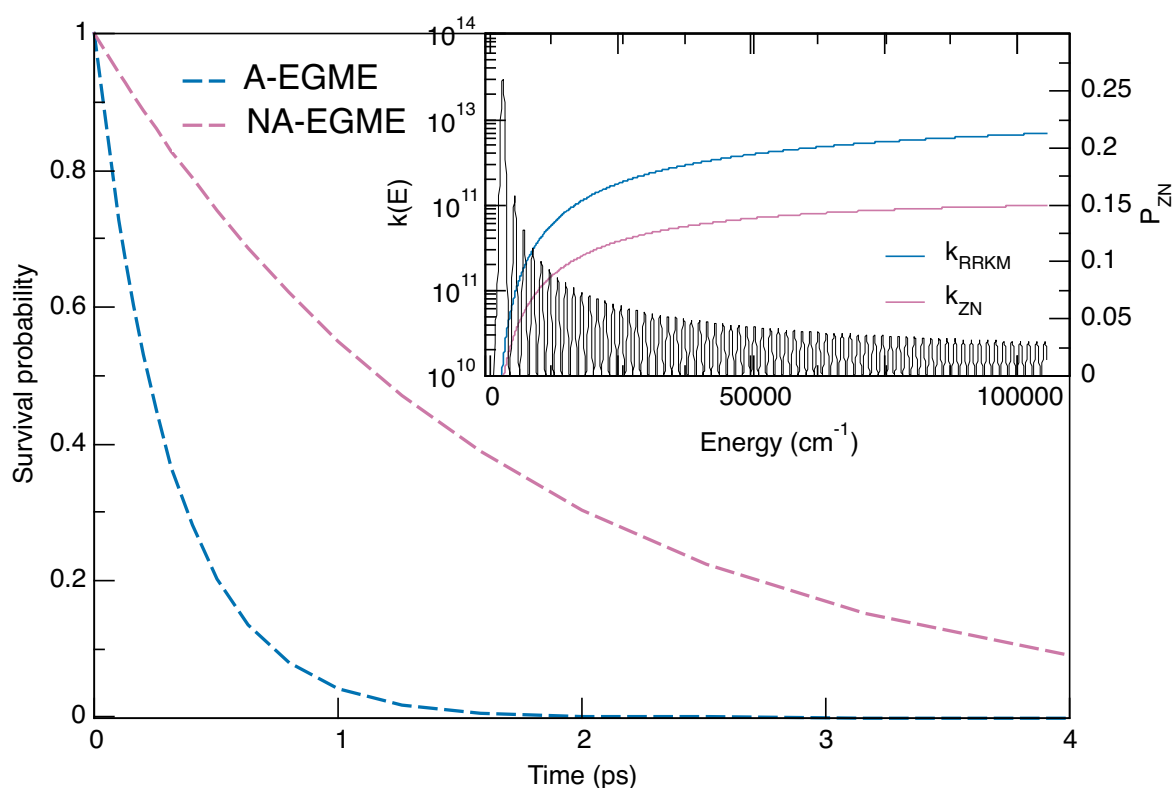


Figure 11: Results of EGME calculations, with microcanonical rates calculated using an adiabatic (A-EGME) and a nonadiabatic (NA-EGME) expression. Inset shows the energy resolved microcanonical rate constants (k_{RRKM} and k_{ZN}) and the ZN transition probability (black line).

An implicit assumption in this treatment of hindered rotations is that rotamer interconversion is fast on the reaction timescale. However, conformational analysis of the trajectories in Figure 9 shows that while internal rotations are present, they are not fast. For this simplified model we make an approximation to consider only the global S_1 minimum (S_1 -B) and a single lowest point on the (3N-7) seam (S_1 -TS). Similarity between the frequencies and rotational constants of the conformers suggest that this is an acceptable compromise in this case.

4.3.3 Correcting the NA-EGME model with MS-CASPT2 energies

Our NA-EGME model could be improved by the addition of all inter-conformer transition states. However, the need to search for each critical point on a 3N dimensional PES can undermine the

simplicity of the approach proposed here. Instead, we can exploit the comparatively low computational cost of the EGME calculations by using energies calculated with a more sophisticated, multireference, electronic structure method at the stationary points. By assuming that the locations of the stationary points optimised with LR-TDDFT give a broadly accurate representation of the PES, the model can be adjusted by using MS(4)-CASPT2(10,8)/6-31G* energies (with LR-TDDFT frequencies and rotational constants) to calculate the population profile of HPALD over time. Results of this scan are shown in Figure 12. New parameters are used in the ZN equations, based on the fitting of diabats to new MS-CASPT2 energies calculated across the same eigenvector coordinate as in the earlier calculation.

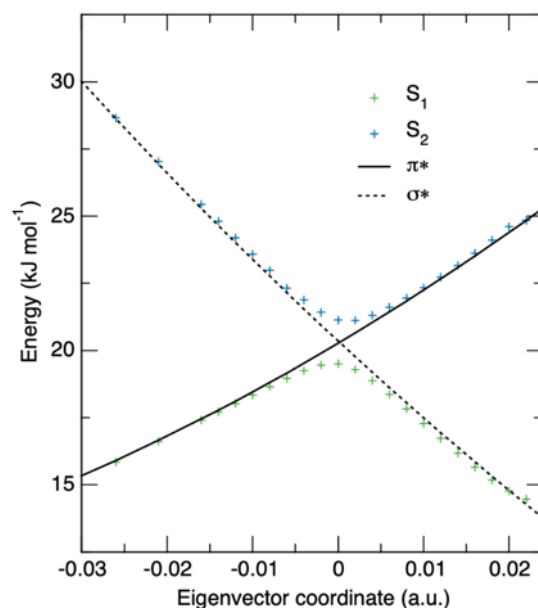


Figure 12: MS(4)-CASPT2(10,8)/6-31G* scan across the S_1 -TS geometry along the eigenvector of the imaginary normal mode, optimised with LR-TDDFT/PBE0/6-31G. Fitted diabatic states used for parameter fitting in the NA-EGME calculation are shown in black

Results of NA-EGME calculations based on MS-CASPT2 energies show that the difference between the nonadiabatic and adiabatic rates is more significant than that produced using TDDFT/PBE0 energies. The adiabatic lifetime of HPALD is $\tau_{A-EGME} = 0.44$ ps whereas the nonadiabatic lifetime, $\tau_{NA-EGME} = 30$ ps, is 70 times slower. Nonadiabatic coupling between the states is weaker increasing the likelihood of transition to the S_2 state, as can be seen in the SI.

5 Discussion

The most direct comparison between the two approaches can be seen in the models that isolate conformer C. Figure 8 demonstrates the remarkable, almost quantitative, similarity between the results of trajectory-based methods and EGME: the FSSH photolysis lifetime $\tau_{FSSH} = 1.9$ ps is comparable to the NA-EGME lifetime $\tau_{NA-EGME} = 2.7$ ps. The impact of nonadiabatic effects on the photolysis rate is stronger in the EGME results: the calculated adiabatic lifetimes are $\tau_{A-EGME} = 0.5$ ps and $\tau_{A-EGME} = 1.29$ ps. A direct comparison between the decay rates in the extended models that include all conformers can be seen in Figure 13. Nonadiabatic EGME and FSSH methods returned lifetimes differing by less than factor of 3: $\tau_{NA-EGME} = 1.7$ ps and $\tau_{FSSH} = 4.6$ ps. These results are still qualitatively similar, which is remarkable given the stark differences between the two approaches. For the adiabatic simulations the comparison is made with the slow component of the fitted decay, with $\tau_{A-EGME} = 0.31$ ps and $\tau_{AIMD} = 2.4$ ps, out by less than a factor of 8. Trajectory surface hopping simulations indicate that a diabatic trapping mechanism is responsible for this deceleration as it causes

the nuclear wavepacket to be trapped in a bound diabatic state, preventing direct dissociation. To quantify the impact of nonadiabatic effects at the seam, for the both the dynamical and the master equation approaches, we compare the ratios of the nonadiabatic/adiabatic lifetimes. This value is 1.9 for the trajectory methods, and 5.5 for the kinetic model. The difference may arise in part from the assumption within the EGME model that allows for only a single seam crossing. It is also important to highlight that the excited-state dynamics performed here assume the formation of a nuclear wavepacket upon light absorption. Such initial condition corresponds to a scenario where the molecule is photoexcited by an ultrashort laser pulse, rather than continuous irradiation with sunlight as it would happen under atmospheric conditions. The question of selecting proper initial conditions for the excited-state dynamics of atmospheric molecules is discussed further in Suchan *et al.*⁴⁵ A protocol aiming at simulating sunlight absorption processes was also recently proposed.⁴⁶ In the context of this work, this assumption does not affect the comparison between the EGME models and the dynamics, but does limit the claims we can make about the atmospheric implications of our results.

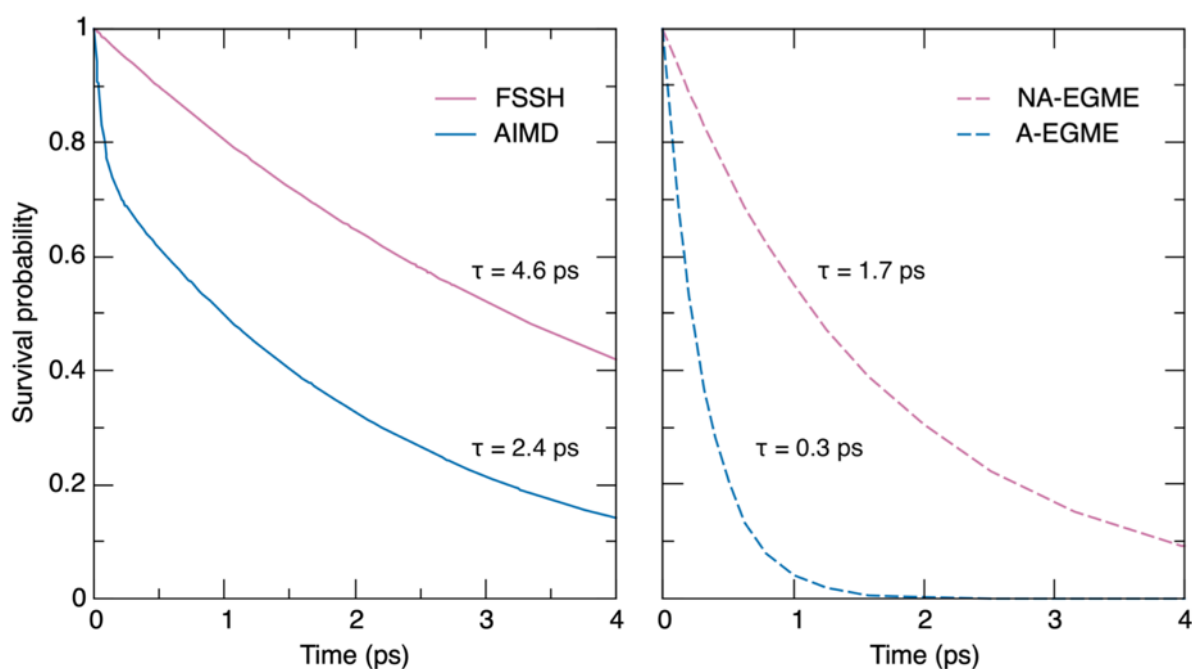


Figure 13: Side-by-side comparison of the two models used to calculate the dissociation rate for C_6 -HPALD. The fit to the population decay is presented for both FSSH and AIMS.

In this paper we aimed to validate a nonadiabatic EGME model against FSSH by calculating the rate of OH loss in C_6 -HPALD, which has been experimentally investigated by Wolfe *et al.*¹⁹ We highlight the approximations made in the construction of the master equation model and outline how this model can be improved. Many features of the C_6 -HPALD dissociation process seem to justify these approximations. This includes the picosecond timescale of photodissociation; ease of energy exchange between the many modes of HPALD; the $(3N-7)$ geometry of the seam which makes the 1-D seam crossing model appropriate. Of course, the exploratory value of running dynamics simulations cannot be superseded by a model that requires existing knowledge of important stationary points. Without performing the FSSH calculations the diabatic trapping mechanism would not have been identified. Nonadiabatic transitions are ultimately caused by nuclear motion and so atomistic simulations are necessary for an accurate description of wavepacket dynamics. However, when nonadiabatic transitions between excited states occur on a slow timescale we are limited by the computational cost of running long trajectories and using the NA-EGME model allows us to refine the energies of the critical points whilst reproducing the overall impact of diabatic trapping on the

photolysis rate. A shorthand calculation of CPU core hours needed to execute both types of calculations tells us that running dynamics cost 200 times more than the NA-EGME approach, including all the preliminary electronic structure calculation of the parameters needed for the model. In instances of slow photodynamic reactions with known mechanisms, alternative models might be explored before choosing to run trajectory dynamics.

The workflow to perform a nonadiabatic EGME analysis on this type of crossing can then be summarised as follows.

1. Locate and characterise the critical points on the excited state PES. These include the bound minima near the FC region, the conical intersections, and the adjacent transition states.
2. Identify the normal mode at the crossing point that corresponds to the exciton moving from one chromophore to the other.
3. Perform a scan across this normal mode and fit diabatic curves to the shape of the crossing point along a 1-dimensional analytical model.
4. Construct an EGME model of the seam crossing, using the fitting parameters obtained in step 3 for ZN transition probabilities. This utility is currently implemented in MESMER.

These findings describe a type of crossing between adiabatic surfaces that is intermediate to the traditional representation of a two-cone type conical intersection (Figure 14, left panel) and a fully degenerate seam one might see in the context of intersystem crossing (Figure 14, right panel). The protocol described here is applicable when calculating rates for this type of trivially unavoided crossing i.e. when collapsing the reaction coordinate to a single dimension is appropriate. These coordinates could be identified through principal component analysis of trajectory dynamics.

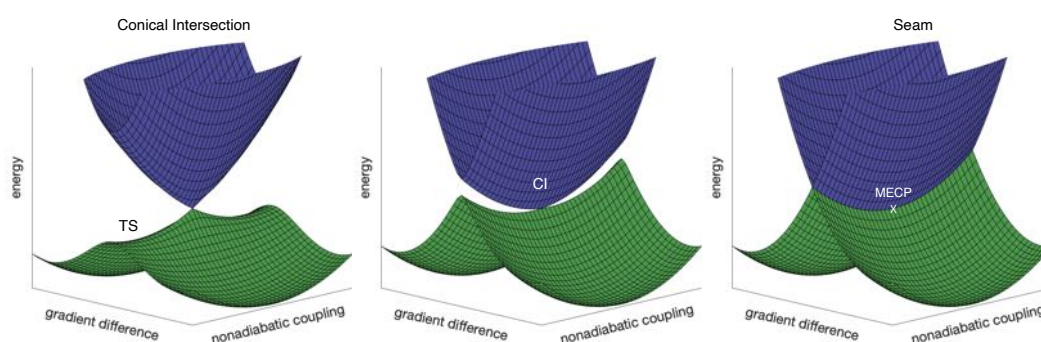


Figure 14: Types of crossings between adiabatic states, the geometry of the intersection is determined by the extent of the nonadiabatic coupling between states. Central panel represents a model topology like that of the $n\pi^*/n'\sigma^*$ crossing in C_6 -HPALD where the CI is only a single point on an extended seam and so becomes less important in the overall description of the nonadiabatic transition.

6. Conclusions

We directly compared the performance of FSSH dynamics to that of a nonadiabatic EGME model by conducting two side-by-side studies of C_6 -HPALD photodissociation. Both methods establish that the nonadiabatic coupling at the extended seam is significant and reduces the rate of OH loss. The lifetimes of C_6 -HPALD based on these fundamentally different models indicate that a reduced dimensionality NA-EGME treatment for avoided crossings can reproduce results of dynamics to within an order of magnitude. Further work is needed to investigate the rate of intra-vibrational relaxation between all modes, so as to determine the exact limits of the regime where this kind of protocol can be applied. Similarity between the dynamic and EGME results also raises the question

of timescale, since intra-vibrational relaxation must be fast to satisfy the key assumption of RRKM theory. It is unclear whether this is satisfied in this case, and so merits further work to investigate the energy redistribution between modes prior to the dissociation. Some purely dynamical features such as loss of HO₂ could not be included in an EGME treatment, and merit further exploration to determine the significance of HO₂ loss to the atmospheric mechanism. Alongside the significant improvement in computational cost we highlight that approaching this photolysis mechanism from both the kinetic and the dynamic perspective offers insights into different aspects of the dissociative process.

Acknowledgements

D.R.G. acknowledges funding from the Royal Society as a University Research Fellow. RJS is supported by EPSRC Programme Grant No. EP/P021123/1. D.S. acknowledges PhD studentship support from the EPSRC Centre for Doctoral Training in Theory and Modelling in Chemical Sciences (EP/L015722/1). This project has received funding from the European Research Council (ERC) under the European Union's Horizon 2020 research and innovation programme (Grant Agreements 803718 and 701355 – Projects SINDAM and NAMDIA). Thanks to Prof. Todd Martinez for useful discussions at various stages.

References

- (a) Lee, M. K.; Coker, D. F., Modeling electronic-nuclear interactions for excitation energy transfer processes in light-harvesting complexes. *J. Phys. Chem. Lett.* **2016**, *7* (16), 3171 - 3178; (b) Sisto, A.; Stross, C.; van der Kamp, M. W.; O'Connor, M.; McIntosh-Smith, S.; Johnson, G. T.; Hohenstein, E. G.; Manby, F. R.; Glowacki, D. R.; Martinez, T. J., Atomistic non-adiabatic dynamics of the LH2 complex with a GPU-accelerated ab initio exciton model. *Phys. Chem. Chem. Phys.* **2017**, *19* (23), 14924-14936; (c) Hayes, D.; Griffin, G. B.; Engel, G. S., Engineering coherence among excited states in synthetic heterodimer systems. *Science* **2013**, *340* (6139), 1431-1434; (d) Sisto, A.; Glowacki, D. R.; Martínez, T. J., Ab initio nonadiabatic dynamics of multichromophore complexes: a scalable graphical-processing-unit-accelerated exciton framework. *Acc. Chem. Res.* **2014**, *47* (9), 2857-2866; (e) Shim, S.; Rebentrost, P.; Valleau, S.; Aspuru-Guzik, A., Atomistic study of the long-lived quantum coherences in the Fenna-Matthews-Olson complex. *Biophys. J* **2012**, *102* (3), 649-660.
- (a) Landau, L. D., A theory of energy transfer II. *Phys. Z. Sowjetunion* **1932**, *2* (46); (b) Zener, C., Non-adiabatic crossing of energy levels. *Proc. R. Soc. Lond.* **1932**, *137* (833); (c) Stückelberg, E. C. G., Theory of Inelastic Collisions between Atoms. *Helv. Phys. Acta* **1932**, *5* (369).
- (a) Nakamura, H., Semiclassical treatment of nonadiabatic transitions: Multilevel curve crossing and nonadiabatic tunneling problems. *J. Chem. Phys.* **1987**, *87* (7), 4031-4041; (b) Zhu, C.; Nakamura, H., Theory of nonadiabatic transition for general two-state curve crossing problems. I. Nonadiabatic tunneling case. *J. Chem. Phys.* **1994**, *101* (12), 10630-10647; (c) Zhu, C.; Nakamura, H., The two-state linear curve crossing problems revisited. II. Analytical approximations for the Stokes constant and scattering matrix: The Landau-Zener case. *J. Chem. Phys.* **1992**, *97* (11), 8497-8514; (d) Zhu, C.; Nakamura, H., The two-state linear curve crossing problems revisited. I. Analysis of Stokes phenomenon and expressions for scattering matrices. *J. Chem. Phys.* **1992**, *97* (3), 1892-1904; (e) Zhu, C.; Nakamura, H., The two-state linear curve crossing problems revisited. III. Analytical approximations for Stokes constant and scattering matrix: Nonadiabatic tunneling case. *J. Chem. Phys.* **1993**, *98* (8), 6208-6222; (f) Zhu, C.; Nakamura, H., Theory of nonadiabatic transition for general two-state curve crossing problems. II. Landau-Zener case. *J. Chem. Phys.*

- 1995**, *102* (19), 7448-7461; (g) Zhu, C.; Nakamura, H., Two-state linear curve crossing problems revisited. IV. The best analytical formulas for scattering matrices. *J. Chem. Phys.* **1994**, *101* (6), 4855-4866.
4. Tully, J. C., Molecular dynamics with electronic transitions. *J. Chem. Phys.* **1990**, *93* (1061).
5. Horenko, I.; Salzmann, C.; Schmidt, B.; Schütte, C., Quantum-classical Liouville approach to molecular dynamics: Surface hopping Gaussian phase-space packets. *J. Chem. Phys.* **2002**, *117*, 11075.
6. (a) Francés-Monerris, A.; Carmona-García, J.; Acuña, A. U.; Dávalos, J. Z.; Cuevas, C. A.; Kinnison, D. E.; Francisco, J. S.; Saiz-Lopez, A.; Roca-Sanjuán, D., Photodissociation mechanisms of major mercury(II) species in the atmospheric chemical cycle of mercury. *Angew. Chem. Int. Ed.* **2020**, *59* (19), 7605–7610; (b) Rodrigues, G. P.; Ventura, E.; Andrade Do Monte, S.; Barbatti, M., Photochemical Deactivation Process of HCFC-133a (C₂H₂F₃Cl): A Nonadiabatic Dynamics Study. *J. Phys. Chem. A* **2014**, *118* (51), 12041 - 12049; (c) Prlj, A.; Ibele, L. M.; Marsili, E.; Curchod, B. F. E., On the theoretical determination of photolysis properties for atmospheric volatile organic compounds. *J. Phys. Chem. Lett.* **2020**, *11* (14), 5418-5425; (d) Shemesh, D.; Gerber, R. B., Femtosecond timescale deactivation of electronically excited peroxides at ice surfaces. *Mol. Phys.* **2012**, *110*, 605 - 617.
7. Westermayr, J.; Gastegger, M.; Menger, F. S. J. M.; Mai, S.; Gonzalez, L.; Marquetand, P., Machine learning enables long time scale molecular photodynamics simulations. *Chem. Sci.* **2019**, *10*, 8100-8107.
8. Blitz, M. A.; Salter, R. J.; Heard, D. E.; Seakins, P. W., An experimental and master equation study of the kinetics of OH/OD + SO₂: the limiting high-pressure rate coefficients. *J. Phys. Chem. A* **2017**, *121* (17), 3184-3191.
9. (a) Goldman, L. M.; Glowacki, D. R.; Carpenter, B. K., Nonstatistical dynamics in unlikely places: [1,5] hydrogen migration in chemically activated cyclopentadiene. *J. Am. Chem. Soc.* **2011**, *133* (14), 5312-5318; (b) Glowacki, D. R.; Liang, C. H.; Marsden, S.; Harvey, J. N.; Pilling, M. J., Alkene hydroboration: hot intermediates that react while they are cooling. *J. Am. Chem. Soc.* **2010**, *132* (39), 13621-13623.
10. Glowacki, D. R.; Rodgers, W. J.; Shannon, R.; Robertson, S. H.; Harvey, J. N., Reaction and relaxation at surface hotspots: using molecular dynamics and the energy-grained master equation to describe diamond etching. *Philos. Trans. R. Soc. A* **2017**, *375* (2092).
11. Bonhommeau, D.; Truhlar, D. G., Mixed quantum/classical investigation of the photodissociation of NH₃(\tilde{A}) and a practical method for maintaining zero-point energy in classical trajectories. *J. Chem. Phys.* **2008**, *129* (1), 014302.
12. Miller, W. H., Tunneling corrections to unimolecular rate constants, with application to formaldehyde. *J. Am. Chem. Soc.* **1979**, *101*, 6810-6814.
13. Garrett, B. C.; Truhlar, D. G., Semiclassical tunneling calculations. *J. Phys. Chem.* **1979**, *83* (22), 2921-2926.
14. (a) Lorquet, J. C.; Leyh-Nihant, B., Nonadiabatic unimolecular reactions. 1. A statistical formulation for the rate constants. *J. Phys. Chem.* **1988**, *92* (16), 4778-4783; (b) Hammes-Schiffer, S.; Tully, J. C., Nonadiabatic transition state theory and multiple potential energy surface molecular dynamics of infrequent events. *J. Chem. Phys.* **1995**, *103* (19), 8528-8537; (c) Lykhin, A. O.; Kaliakin, D. S.; dePolo, G. E.; Kuzubov, A. A.; Varganov, S. A., Nonadiabatic transition state theory: application to intersystem crossings in the active sites of metal-sulfur proteins. *Int. J. Quantum Chem.* **2016**, *116* (10), 750-761.
15. (a) Harvey, J. N.; Aschi, M., Modelling spin-forbidden reactions: recombination of carbon monoxide with iron tetracarbonyl. *Faraday Discuss.* **2003**, *124*, 129-143; (b) Harvey, J. N., Understanding the kinetics of spin-forbidden chemical reactions. *Phys. Chem. Chem. Phys.* **2006**, *9*, 331-343; (c) Zaari, R. R.; Varganov, S. A., Nonadiabatic transition state theory and trajectory

- surface hopping dynamics: intersystem crossing between 3B_1 and 1A_1 states of SiH_2 . *J. Phys. Chem. A* **2015**, *119* (8), 1332-1338; (d) Lykhin, A. O.; Varganov, S. A., Intersystem crossing in tunneling regime: $T_1 \rightarrow S_0$ relaxation in thiophosgene. *Phys. Chem. Chem. Phys.* **2020**, *22* (10), 5500-5508.
16. Maiti, B.; Schatz, G. C.; Lendvay, G., Importance of intersystem crossing in the $S(^3P, ^1D) + H_2 \rightarrow SH + H$ reaction. *J. Phys. Chem. A* **2004**, *108* (41), 8772-8781.
17. Granucci, G.; Persico, M.; Spighi, G., Surface hopping trajectory simulations with spin-orbit and dynamical couplings. *J. Chem. Phys.* **2012**, *137* (22).
18. (a) Richter, M.; Marquetand, P.; González-Vázquez, J.; Sola, I.; González, L., SHARC – ab initio molecular dynamics with surface hopping in the adiabatic representation including arbitrary couplings. *J. Chem. Theory Comput.* **2011**, *7* (5), 1253-1258; (b) Mai, S.; Marquetand, P.; Gonzalez, L., A general method to describe intersystem crossing dynamics in trajectory surface hopping. *Int. J. Quantum Chem.* **2015**, *115* (18), 1215-1231.
19. Wolfe, G. D.; Crouse, J. D.; Parrish, J. D.; St. Clair, J. M.; Beaver, M. R.; Paulot, F.; Yoon, T. P.; Wennberg, P. O.; Keutsch, F. N., Photolysis, OH reactivity and ozone reactivity of a proxy for isoprene-derived hydroperoxyenals (HPALDs). *Phys. Chem. Chem. Phys.* **2012**, *14*, 7276-7286.
20. (a) Peeters, J.; Müller, J.-F.; Stavrou, T.; Nguyen, V. S., Hydroxyl radical recycling in isoprene oxidation driven by hydrogen bonding and hydrogen tunneling: the upgraded LIM1 mechanism. *J. Phys. Chem. A* **2014**, *118*, 8625-8643; (b) Peeters, J.; Muller, J. F., HOx radical regeneration in isoprene oxidation via peroxy radical isomerisations. II: experimental evidence and global impact. *Phys. Chem. Chem. Phys.* **2010**, *12* (42), 14227-14235; (c) Peeters, J.; Nguyen, T. L.; Vereecken, L., HOx radical regeneration in the oxidation of isoprene. *Phys. Chem. Chem. Phys.* **2009**, *11* (28), 5935-9; (d) Taraborrelli, D.; Lawrence, M. G.; Crowley, J. N.; Dillon, T. J.; Gromov, S.; Groß, C. B. M.; Vereecken, L.; Lelieveld, J., Hydroxyl radical buffered by isoprene oxidation over tropical forests. *Nature Geosci.* **2012**, *5* (3), 190-193; (e) Lelieveld, J.; Butler, T. M.; Crowley, J. N.; Dillon, T. J.; Fischer, H.; Ganzeveld, L.; Harder, H.; Lawrence, M. G.; Martinez, M.; Taraborrelli, D.; Williams, J., Atmospheric oxidation capacity sustained by a tropical forest. *Nature* **2008**, *452* (7188), 737-740; (f) Hansen, R. F.; Lewis, T. R.; Graham, L.; Whalley, L. K.; Seakins, P. W.; Heard, D. E.; Blitz, M. A., OH production from the photolysis of isoprene-derived peroxy radicals: cross-sections, quantum yields and atmospheric implications. *Phys. Chem. Chem. Phys.* **2017**, *19*, 2332-2345.
21. (a) Glowacki, D. R.; Lockhart, J.; Blitz, M. A.; Klippenstein, S. J.; Pilling, M. J.; Robertson, S. H.; Seakins, P. W., Interception of excited vibrational quantum states by O_2 in atmospheric association reactions. *Science* **2012**, *337* (6098), 1066-1069; (b) Plane, J. M. C.; Whalley, C. L.; Frances-Soriano, L.; Goddard, A.; Harvey, J. N.; Glowacki, D. R.; Viggiano, A. A., $O_2(a^1\Delta_g) + Mg, Fe, \text{ and } Ca$: Experimental kinetics and formulation of a weak collision, multiwell master equation with spin-hopping. *J. Chem. Phys.* **2012**, *137*, 014310; (c) Vereecken, L.; Glowacki, D. R.; Pilling, M. J., Theoretical chemical kinetics in tropospheric chemistry: methodologies and applications. *Chem. Rev.* **2015**, *115* (10), 4063-4114.
22. Nakamura, H., Dynamics of nonadiabatic chemical reactions. *J. Phys. Chem. A* **2006**, *110* (38), 10929-10946.
23. Glowacki, D. R.; Lightfoot, R.; Harvey, J. N., Non-equilibrium phenomena and molecular reaction dynamics: mode space, energy space and conformer space. *Mol. Phys.* **2013**, *111* (5), 631-640.
24. Robertson, S. H.; Glowacki, D. R.; Liang, C.-H.; Morley, C.; Shannon, R.; Blitz, M.; Pilling, M. J. *MESMER v6.0 (master equation solver for multi energy well reactions)*, 2020.
25. Tozer, D. J., Relationship between long-range charge-transfer excitation energy error and integer discontinuity in Kohn–Sham theory. *J. Chem. Phys.* **2003**, *119* (12697).
26. Levine, B. G.; Ko, C.; Quenneville, J.; Martinez, T. J., Conical intersections and double excitations in time-dependent density functional theory. *Mol. Phys.* **2006**, *104* (5-7).

27. (a) Agostini, F.; Curchod, B. F. E.; Vuilleumier, R.; Tavernelli, I.; Gross, E. K. U., TDDFT and quantum-classical dynamics: a universal tool describing the dynamics of matter. In *Handbook of Materials Modeling: Methods: Theory and Modeling*, Andreoni, W.; Yip, S., Eds. Springer International Publishing: Cham, 2020; pp 75-121; (b) Curchod, B. F. E.; Rothlisberger, U.; Tavernelli, I., Trajectory-based nonadiabatic dynamics with time-dependent density functional theory. *Chem. Phys. Chem. Rev.* **2013**, *14* (7), 1314-1340.
28. Frisch, M. J.; Trucks, G. W.; Schlegel, H. B.; Scuseria, G. E.; Robb, M. A.; Cheeseman, J. R.; Scalmani, G.; Barone, V.; Petersson, G. A.; Nakatsuji, H.; Li, X.; Caricato, M.; Marenich, A. V.; Bloino, J.; Janesko, B. G.; Gomperts, R.; Mennucci, B.; Hratchian, H. P.; Ortiz, J. V.; Izmaylov, A. F.; Sonnenberg, J. L.; Williams-Young, D.; Ding, F.; Lipparini, F.; Egidi, F.; Goings, J.; Peng, B.; Petrone, A.; Henderson, T.; Ranasinghe, D.; Zakrzewski, V. G.; Gao, J.; Rega, N.; Zheng, G.; Liang, W.; Hada, M.; Ehara, M.; Toyota, K.; Fukuda, R.; Hasegawa, J.; Ishida, M.; Nakajima, T.; Honda, Y.; Kitao, O.; Nakai, H.; Vreven, T.; Throssell, K.; Montgomery, J. A., Jr.; Peralta, J. E.; Ogliaro, F.; Bearpark, M. J.; Heyd, J. J.; Brothers, E. N.; Kudin, K. N.; Staroverov, V. N.; Keith, T. A.; Kobayashi, R.; Normand, J.; Raghavachari, K.; Rendell, A. P.; Burant, J. C.; Iyengar, S. S.; Tomasi, J.; Cossi, M.; Millam, J. M.; Klene, M.; Adamo, C.; Cammi, R.; Ochterski, J. W.; Martin, R. L.; Morokuma, K.; Farkas, O.; Foresman, J. B.; Fox, D. J. *Gaussian 16, Revision C.01*, Gaussian, Inc.: Wallingford CT, 2016.
29. Werner, H.-J.; Knowles, P. J.; Knizia, G.; Manby, F. R.; Schütz, M.; Celani, P.; Györffy, W.; Kats, D.; Korona, T.; Lindh, R.; Mitrushenkov, A.; Rauhut, G.; Shamasundar, K. R.; Adler, T. B.; Amos, R. D.; Bennie, S. J.; Bernhardsson, A.; Berning, A.; Cooper, D. L.; Deegan, M. J. O.; Dobbyn, A. J.; Eckert, F.; Goll, E.; Hampel, C.; Hesselmann, A.; Hetzer, G.; Hrenar, T.; Jansen, G.; Köppl, C.; Lee, S. J. R.; Liu, Y.; Lloyd, A. W.; Ma, Q.; Mata, R. A.; May, A. J.; McNicholas, S. J.; Meyer, W.; III, T. F. M.; Mura, M. E.; Nicklass, A.; O'Neill, D. P.; Palmieri, P.; Peng, D.; Pflüger, K.; Pitzer, R.; Reiher, M.; Shiozaki, T.; Stoll, H.; Stone, A. J.; Tarroni, R.; Thorsteinsson, T.; Wang, M.; Welborn, M. *MOLPRO, version 2019.2, a package of ab initio programs*, 2019.
30. Galván, I. F.; Vacher, M.; Alavi, A.; Angeli, C.; Aquilante, F.; Autschbach, J.; Bao, J. J.; Bokarev, S. I.; Bogdanov, N. A.; Carlson, R. K.; Chibotaru, L. F.; Creutzberg, J.; Dattani, N.; Delcey, M. G.; Dong, S. S.; Dreuw, A.; Freitag, L.; Frutos, L. M.; Gagliardi, L.; Gendron, F.; Giussani, A.; González, L.; Grell, G.; Guo, M.; Hoyer, C. E.; Johansson, M.; Keller, S.; Knecht, S.; Kovačević, G.; Kállman, E.; Manni, G. L.; Lundberg, M.; Ma, Y.; Mai, S.; Malhado, J. P.; Malmqvist, P. Å.; Marquetand, P.; Mewes, S. A.; Norell, J.; Olivucci, M.; Oppel, M.; Phung, Q. M.; Pierloot, K.; Plasser, F.; Reiher, M.; Sand, A. M.; Schapiro, I.; Sharma, P.; Stein, C. J.; Sørensen, L. K.; Truhlar, D. G.; Ugandi, M.; Ungur, L.; Valentini, A.; Vancoillie, S.; Veryazov, V.; Weser, O.; Wesołowski, T. A.; Widmark, P.-O.; Wouters, S.; Zech, A.; Zobel, J. P.; Lindh, R., OpenMolcas: from source code to insight. *J. Chem. Theory Comput.* **2019**, *15* (11), 5925-5964.
31. Harvey, J. N.; Aschi, M.; Schwarz, H.; Koch, W., The singlet and triplet states of phenyl cation. A hybrid approach for locating minimum energy crossing points between non-interacting potential energy surfaces. *Theo. Chem. Acc.* **1997**, *99*, 95-99.
32. Crespo-Otero, R.; Barbatti, M., Spectrum simulation and decomposition with nuclear ensemble: Formal derivation and application to benzene, furan and 2-phenylfuran. *Theo. Chem. Acc.* **2012**, *131* (6), 1-14.
33. Barbatti, M.; Granucci, G.; Persico, M.; Ruckebauer, M.; Vazdar, M.; Eckert-Maksić, M.; Lischka, H., The on-the-fly surface-hopping program system Newton-X: application to ab initio simulation of the nonadiabatic photodynamics of benchmark systems. *J. Photochem. Photobiol. A* **2007**, *190*, 228-240.
34. Frisch, M. J.; Trucks, G. W.; Schlegel, H. B.; Scuseria, G. E.; Robb, M. A.; Cheeseman, J. R.; Scalmani, G.; Barone, V.; Mennucci, B.; Petersson, G. A.; Nakatsuji, H.; Caricato, M.; Li, X.; Hratchian, H. P.; Izmaylov, A. F.; Bloino, J.; Zheng, G.; Sonnenberg, J. L.; Hada, M.; Ehara, M.; Toyota, K.; Fukuda, R.; Hasegawa, J.; Ishida, M.; Nakajima, T.; Honda, Y.; Kitao, O.; Nakai, H.;

Vreven, T.; Montgomery, J. A., Jr.; Peralta, J. E.; Ogliaro, F.; Bearpark, M.; Heyd, J. J.; Brothers, E.; Kudin, K. N.; Staroverov, V. N.; Kobayashi, R.; Normand, J.; Raghavachari, K.; Rendell, A.; Burant, J. C.; Iyengar, S. S.; Tomasi, J.; Cossi, M.; Rega, N.; Millam, J. M.; Klene, M.; Knox, J. E.; Cross, J. B.; Bakken, V.; Adamo, C.; Jaramillo, J.; Gomperts, R.; Stratmann, R. E.; Yazyev, O.; Austin, A. J.; Cammi, R.; Pomelli, C.; Ochterski, J. W.; Martin, R. L.; Morokuma, K.; Zakrzewski, V. G.; Voth, G. A.; Salvador, P.; Dannenberg, J. J.; Dapprich, S.; Daniels, A. D.; Farkas, Ö.; Foresman, J. B.; Ortiz, J. V.; Cioslowski, J.; Fox, D. J. *Gaussian 09, Revision A.02*, Gaussian, Inc.: Wallingford CT, 2016.

35. Granucci, G.; Persico, M., Critical appraisal of the fewest switches algorithm for surface hopping. *J. Chem. Phys.* **2007**, *126* (13), 134114.
36. Pittner, J.; Lischka, H.; Barbatti, M., Optimization of mixed quantum-classical dynamics: time-derivative coupling terms and selected couplings. *Chem. Phys.* **2009**, *356* (1-3), 147-152.
37. Holbrook, K. A.; Pilling, M. J.; Robertson, S. H., *Unimolecular Reactions*. Wiley: Chichester, 1996.
38. Glowacki, D. R.; Liang, C.-H.; Morley, C.; Pilling, M. J.; Robertson, S. H., MESMER: an open-source master equation solver for multi-energy well reactions. *J. Phys. Chem. A* **2012**, *116*, 9545-9560.
39. (a) Lasorne, B.; Bacchus-Montabonel, M.-C.; Vaeck, N.; Desouter-Lecomte, M., Nonadiabatic interactions in wave packet dynamics of the bromoacetyl chloride photodissociation. *J. Chem. Phys.* **2004**, *120* (3), 1271-1278; (b) Martínez, T. J., Ab initio molecular dynamics around a conical intersection: Li(2p) + H₂. *Chem. Phys. Lett.* **1997**, *272* (3), 139-147.
40. Blancafort, L.; Hunt, P.; Robb, M. A., Intramolecular electron transfer in bis(methylene) adamantyl radical cation: a case study of diabatic trapping. *J. Am. Chem. Soc.* **2005**, *127* (10), 3391-3399.
41. Baasandorj, M.; Papanastasiou, D. K.; Talukdar, R. K.; Hasson, A. S.; Burkholder, J. B., (CH₃)₃COOH (tert-butyl hydroperoxide): OH reaction rate coefficients between 206 and 375 K and the OH photolysis quantum yield at 248 nm. *Phys. Chem. Chem. Phys.* **2010**, *12*, 12101-12111.
42. Glowacki, D. R.; Reed, S. K.; Pilling, M. J.; Shalashilin, D. V.; Martínez-Núñez, E., Classical, quantum and statistical simulations of vibrationally excited HOSO₂: IVR, dissociation, and implications for OH + SO₂ kinetics at high pressures. *Phys. Chem. Chem. Phys.* **2009**, *11* (6), 963-974.
43. Zheng, J.; Truhlar, D. G., Multi-path variational transition state theory for chemical reaction rates of complex polyatomic species: ethanol + OH reactions. *Faraday Discuss.* **2012**, *157*, 59.
44. Sharma, S.; Raman, S.; Green, W. H., Intramolecular hydrogen migration in alkylperoxy and hydroperoxyalkylperoxy radicals: accurate treatment of hindered rotors. *J. Phys. Chem. A* **2010**, *114* (18), 5689-5701.
45. Suchan, J.; Hollas, D.; Curchod, B. F. E.; Slavíček, P., On the importance of initial conditions for excited-state dynamics. *Faraday Discuss.* **2018**, *212*, 307-330.
46. Barbatti, M., Simulation of excitation by sunlight in mixed quantum-classical dynamics. *J. Chem. Theo. Comput.* **2020**, *16* (8), 4849-4856.

Supporting Information for

Dynamics in multi-chromophore systems: Nonadiabatic versus energy grained master equation treatments

Darya Shechpanovska, Robin J. Shannon, Basile F. E. Curchod*, and David R. Glowacki*

*glowacki@bristol.ac.uk; basile.f.curchod@durham.ac.uk

S1. Optimised geometries of C₆-HPALD conformers

The chemical structure of the C₅-HPALD proxy, C₆-HPALD, was taken from Wolfe *et al.*¹ Geometry optimisations of the (E)-4-Hydroperoxyhex-2-enal structures were initialised from the 7 distinct conformers A-G (2 rotatable bonds) generated by the systematic rotor search algorithm in Avogadro V1.2.0². The resulting conformers were pre-optimised in Avogadro with the UFF forcefield via the steepest descent algorithm.

The geometry optimizations for all 7 conformers were then performed with LR-TDDFT (PBE0/TZVP) as implemented in Gaussian 16³ with frequencies calculated at the same level.

Optimised geometries of all 7 conformers are presented here (in Angstrom):

A				B			
C	2.9961760000	-1.2969820000	0.1292600000	C	-1.2915260000	2.4517500000	0.2002250000
C	1.5313620000	-1.2598110000	-0.2770690000	C	-1.7351460000	1.1407600000	-0.4277020000
H	3.5474400000	-0.4583130000	-0.2981830000	H	-1.4939960000	2.4670250000	1.2747310000
H	3.4662400000	-2.2203780000	-0.2156750000	H	-1.8278840000	3.2895140000	-0.2494580000
H	3.1048560000	-1.2548880000	1.2167460000	H	-0.2227680000	2.6255210000	0.0589530000
H	1.4330740000	-1.3172610000	-1.3655990000	H	-2.8118440000	1.0018510000	-0.2930580000
C	0.7986030000	-0.0108520000	0.2065270000	C	-1.0430520000	-0.0789720000	0.1781110000
H	1.0004470000	-2.1241120000	0.1316410000	H	-1.5487480000	1.1488550000	-1.5055890000
O	1.4325020000	1.0732750000	-0.4568590000	O	-1.7228770000	-1.1889690000	-0.3914370000
H	0.9314020000	0.1030380000	1.2907210000	H	-1.1851750000	-0.0854660000	1.2670720000
C	-0.6546380000	-0.0702540000	-0.1306310000	C	0.4116430000	-0.1159770000	-0.1514400000
C	-1.6324830000	-0.2126420000	0.7623700000	C	1.3956710000	0.0599570000	0.7287610000
C	-3.0474550000	-0.3124890000	0.3605390000	C	2.8136420000	0.0521150000	0.3245380000
O	-3.4399140000	-0.3389510000	-0.7808060000	O	3.2053030000	-0.0326240000	-0.8142220000
H	-0.9108440000	-0.0116850000	-1.1870720000	H	0.6649910000	-0.2818700000	-1.1973500000
H	-1.4189440000	-0.2445090000	1.8280760000	H	1.1846850000	0.1977140000	1.7863600000
H	-3.7718670000	-0.3625550000	1.1993780000	H	3.5408680000	0.1297690000	1.1588080000
O	0.8811420000	2.2867190000	0.0715100000	O	-1.1855550000	-2.3790760000	0.2030320000
H	1.6789750000	2.7004970000	0.4232240000	H	-1.9824880000	-2.7453530000	0.6055990000
C				D			
C	-0.9626170000	2.4087570000	0.0493740000	C	1.7008540000	-1.9923070000	-0.6162310000
C	-1.4524880000	1.0798020000	-0.5019210000	C	1.6396660000	-1.1796140000	0.6686030000
H	-1.1915480000	2.5023280000	1.1148550000	H	0.7056500000	-2.2855950000	-0.9577790000
H	-1.4456830000	3.2416910000	-0.4652870000	H	2.2744530000	-2.9074780000	-0.4552700000
H	0.1168130000	2.5243320000	-0.0719710000	H	2.1820740000	-1.4303740000	-1.4182820000
H	-2.5378360000	1.0124430000	-0.3900300000	H	1.1215970000	-1.7435210000	1.4496290000
C	-0.8530890000	-0.1286900000	0.2153540000	C	0.9321070000	0.1722800000	0.5486510000
H	-1.2292260000	0.9996760000	-1.5710370000	C	2.6506740000	-0.9822160000	1.0381780000
O	-1.4467810000	-1.3541840000	-0.2104690000	O	1.7388400000	0.9342790000	-0.3374190000
H	-0.9972300000	-0.0278350000	1.2981760000	H	0.9240410000	0.6565450000	1.5340080000
C	0.5943750000	-0.2953170000	-0.1005200000	C	-0.4666170000	0.0469760000	0.0404700000
C	1.5909510000	-0.0460360000	0.7472720000	C	-1.5535840000	0.1428450000	0.8047050000
C	3.0034310000	-0.1856370000	0.3427830000	C	-2.9096150000	-0.0376900000	0.2562350000
O	3.3755010000	-0.4512050000	-0.7742270000	O	-3.1567650000	-0.3502960000	-0.8834010000
H	0.8387060000	-0.6152530000	-1.1120480000	H	-0.5896570000	-0.1525180000	-1.0216090000
H	1.3971450000	0.2544590000	1.7735930000	H	-1.4774590000	0.3764310000	1.8641430000
H	3.7428510000	-0.0311660000	1.1548300000	H	-3.7351560000	0.1389270000	0.9762470000
O	-2.7959590000	-1.3651860000	0.2730490000	O	1.1682830000	2.2460050000	-0.4256510000
H	-3.2794620000	-1.4933500000	-0.5519580000	H	1.8840430000	2.7749570000	-0.0521030000

E				F			
C	-1.3526350000	2.0387340000	-0.3643280000	C	2.9648410000	-1.1647090000	-0.2358960000
C	-1.3805160000	1.0284220000	0.7716990000	C	1.5152760000	-0.9354240000	-0.6306310000
H	-0.3323570000	2.3303710000	-0.6243060000	H	3.4753730000	-0.2175890000	-0.0554490000
H	-1.8924430000	2.9457610000	-0.0846670000	H	3.4995130000	-1.6930910000	-1.0280610000
H	-1.8213030000	1.6366780000	-1.2659070000	H	3.0393900000	-1.7652140000	0.6752780000
H	-0.8483880000	1.4206030000	1.6438300000	H	1.4594590000	-0.3612860000	-1.5590510000
C	-0.7654480000	-0.3304830000	0.4292630000	C	0.7174820000	-0.2025360000	0.4433020000
H	-2.4090660000	0.8439540000	1.0945150000	H	1.0120990000	-1.8890130000	-0.8188520000
O	-1.4398910000	-0.9806270000	-0.6470000000	O	1.3201840000	1.0342890000	0.8261280000
H	-0.8165790000	-0.9792380000	1.3113540000	H	0.7711230000	-0.7627650000	1.3839250000
C	0.6478570000	-0.2158170000	-0.0354020000	C	-0.7088850000	-0.0074620000	0.0490840000
C	1.7119530000	-0.4284220000	0.7373710000	C	-1.7430700000	-0.6439900000	0.5979940000
C	3.0845770000	-0.2431020000	0.2298270000	C	-3.1269330000	-0.4135980000	0.1424660000
O	3.3613670000	0.1701540000	-0.8700140000	O	-3.4427090000	0.3457990000	-0.7415080000
H	0.8088070000	0.0889570000	-1.0671080000	H	-0.9024240000	0.6946490000	-0.7592970000
H	1.6062080000	-0.7581940000	1.7678450000	H	-1.6029250000	-1.3559360000	1.4080540000
H	3.8900450000	-0.5184960000	0.9408090000	H	-3.9030540000	-0.9965230000	0.6793460000
O	-2.7413040000	-1.3446490000	-0.1741940000	O	1.4391110000	1.8615500000	-0.3410440000
H	-3.3010340000	-0.8654220000	-0.7972770000	H	0.9064890000	2.6199760000	-0.0724180000
G							
C	1.6540730000	-1.6353030000	-0.9174200000				
C	1.6073130000	-1.1682290000	0.5303910000				
H	0.6520370000	-1.8249490000	-1.3105530000				
H	2.2133920000	-2.5711840000	-0.9865940000				
H	2.1360410000	-0.9010580000	-1.5616630000				
H	1.1581160000	-1.9546760000	1.1468340000				
C	0.8237120000	0.1147800000	0.8261750000				
H	2.6199440000	-1.0113810000	0.9152730000				
O	1.5505040000	1.3113090000	0.5507330000				
H	0.7211080000	0.1967430000	1.9139350000				
C	-0.5313800000	0.1412620000	0.1999690000				
C	-1.6677700000	-0.1330720000	0.8401490000				
C	-2.9703210000	-0.1102720000	0.1486680000				
O	-3.1238190000	0.1441090000	-1.0216350000				
H	-0.5821360000	0.3841850000	-0.8584960000				
H	-1.6766160000	-0.3813820000	1.8989710000				
H	-3.8466450000	-0.3462560000	0.7865340000				
O	1.7913860000	1.4074100000	-0.8614390000				
H	1.3664340000	2.2523410000	-1.0530990000				

S2. C₆-HPALD conformer energies and Boltzmann weights

Energies of these geometries were then refined at df-CCSD(T)-F12/cc-pVDZ-f12 with def2-QZVPP basis set used for the density fitting, as in the calculations reported in Peeters *et al.*⁴. The energies calculated with df-CCSD(T) are those used to calculate conformer weights in the final run. The Boltzmann weight of conformer *i* with energy E_i at 298K was calculated with the following formula (where E_{min} is the energy of the most stable conformer).

$$w_i = \frac{e^{-(E_i - E_{min})/kT}}{\sum_i^{N_{conf}} e^{-(E_i - E_{min})/kT}}$$

The resulting weights are presented in this table (Energies from df-CCSD(T))

Table S1 Conformer weights calculated from energies computed with df-CCSD(T)-F12/cc-pVDZ-f12/def2-QZVPP

Conformer	Energy (a.u.)	Weight	No of trajectories ran	No trajectories used in analysis
A	-459.6193492	0.224	50	24
B	-459.6193492	0.459	50	50
C	-459.6179138	0.049	10	5

D	-459.6189484	0.146	20	16
E	-459.61729	0.025	5	3
F	-459.6185605	0.097	20	11
G	-459.6148756	0.002	0	0

S3. Electronic structure benchmarks for C₆-HPALD

Calculating properties of excited states, such as excited state energies, nuclear gradients, and nonadiabatic couplings (NAC) for larger molecules can be done accurately and efficiently with linear response (LR-)TDDFT. TDDFT is a single reference method and is formally exact. Its shortfalls are well documented, including its tendency to underestimate energies of states with high charge transfer character⁵ or regions of the PES with strong coupling between ground and excited states⁶. Nevertheless, it is widely used for nonadiabatic dynamics simulations of larger systems due to its favourable computational cost.

Benchmarking employed a number of electronic structure methods which included DFT, LR-TDDFT, CIS, CIS(D), ADC(2), EOM-CCSD, SA-CASSCF, and MS-CASPT2. All DFT, LR-TDDFT, CIS, and CIS(D) calculations were performed in Gaussian 16³. CC2 and ADC(2) calculations were performed in Turbomole v7.1⁷. The EOM-CCSD calculation is executed in Molpro 2018⁸. CASSCF and MS-CASPT2 calculations were performed in OpenMolcas v18.09⁹. The active space contained 10 electrons in 8 orbitals which includes σ/σ^* orbitals at the peroxide bond, π/π^* orbitals at the enone chromophore, and lone pairs on oxygen atoms.

All benchmarks were calculated for $n=5$ except CASSCF and MS-CASPT2 which were calculated for $n=3$.

Table S2 Excitation energies in eV for the first n singlet states at the PBE0/TZVP optimised S₀ geometry of conformer B.

Method	Basis Set	S ₁	S ₂	S ₃	S ₄	S ₅
CIS	6-31G	4.4425	6.7454	6.7915	8.3597	8.3927
	6-311+G*	4.6675	6.4277	6.9813	7.9840	8.2861
	6-311++G**	4.6457	6.4155	6.9665	7.7852	8.2444
CIS(D)	6-31G	3.9083	6.6660	6.8104	7.7418	7.9101
	6-311+G*	3.7471	6.1951	6.4346	6.9162	7.6128
	6-311++G**	3.7468	6.1739	6.4064	6.9186	7.3769
ω B97XD	6-31G	3.6468	5.7016	6.0060	6.1120	6.9943
	6-311+G*	3.6694	5.6377	5.8160	6.1112	6.9448
	6-311++G**	3.6461	5.6161	5.8004	6.0781	6.9032
PBE0	6-31G	3.5260	4.8622	5.8700	5.9635	6.2205
	6-311+G*	3.5291	4.8701	5.6063	5.9754	6.1971
	6-311++G**	3.5046	4.8478	5.5920	5.9338	6.1755
LC- ω PBE	6-31G	3.6944	6.0125	6.2462	6.6052	7.4603
	6-311+G*	3.7482	5.9197	6.1152	6.5375	7.4241
	6-311++G**	3.7245	5.9069	6.0937	6.5056	7.2600
CAM-B3LYP	6-31G	3.6584	5.7352	5.9908	6.1034	7.0161
	6-311+G*	3.6840	5.6435	5.8159	6.0484	6.9394
	6-311++G**	3.6599	5.6240	5.7978	6.0136	6.8136
CC2	cc-pVDZ	3.8107	5.9433	6.4220	6.4997	7.4003
ADC(2)	cc-pVDZ	3.6180	5.9074	6.3592	6.4981	7.3464
	cc-pVTZ	3.5412	5.7588	6.1160	6.3720	7.1849
	cc-pVQZ	3.5151	5.7238	6.0326	6.2971	7.1033
	aug-cc-pVDZ	3.4504	5.5908	5.8035	5.9428	6.0525
EOM-CCSD	aug-cc-pVDZ	3.756	6.114	6.156	6.479	6.852
SA(4)-CASSCF(8/10)	6-31G*	2.63	6.22	6.62	-	-

MS(4)-CASPT2(8/10)	6-31G*	3.70	7.15	8.17	-	-
--------------------	--------	------	------	------	---	---

Rigid scans along the -O--OH coordinate of C₆-HPALD initiated at the optimised PBE0/TZVP S₀ geometry of conformer B.

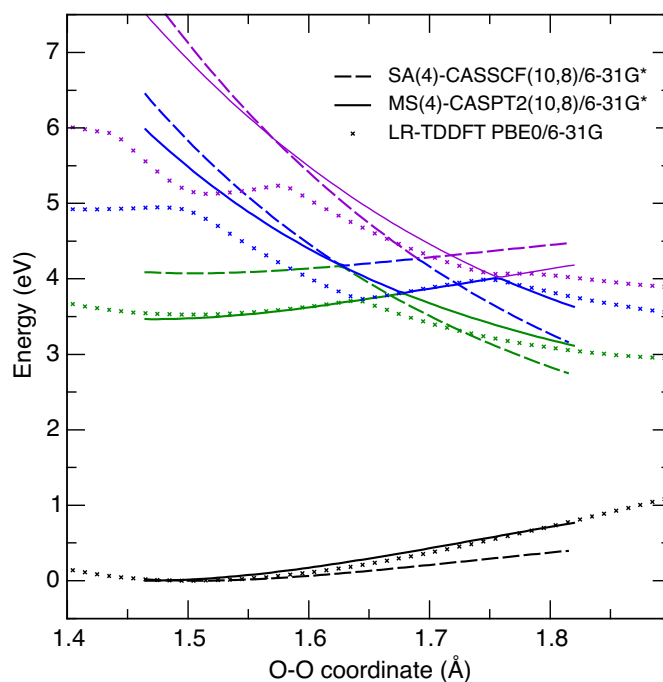


Figure S15 Benchmark scan showing profiles of the first 4 singlet states calculated with LR-TDDFT/PBE0/6-31G; CASSCF(10,8)/6-31G*; MS(4)-CASPT2(10,8)/6-31G*.

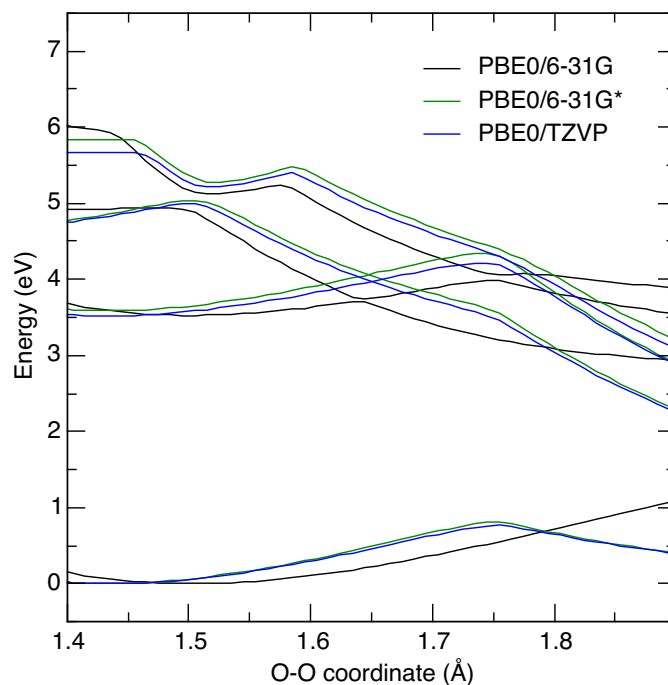


Figure S16 Benchmark scan showing profiles of the first 4 singlet states calculated with LR-TDDFT/PBE0 using basis sets 6-31G, 6-31G*, and TZVP.

S4. Photoabsorption cross section of C₆-HPALD

The photoabsorption cross section $\sigma(\lambda)$ is calculated using the Wigner ensemble sampling method described in Crespo-Otero *et al.*¹⁰ which captures the inhomogeneous broadening of the spectral bands. Harmonic ground state frequencies used to generate the Wigner distribution were calculated for each conformer with DFT/PBE0/6-31G. Distribution assumes temperature of 0 K. For each of 7 conformers, 100 points are sampled from their respective distribution. We calculate the absorption in the 300-400nm range into the S₁ and S₂ electronic states separately, and the combined spectrum. For each sample point the vertical transitions and oscillator strengths are calculated with LR-TDDFT/PBE0/TZVP. Each peak is overlaid with a Lorentzian curve whose phenomenological broadening is set to 0.05 eV to return a continuous spectrum. The final photoabsorption cross section shown in Figure S3 is a linear combination of the spectra for each conformer $\sigma(\lambda) = \sum_i w_i \sigma_i(\lambda)$ where the weights w_i are given in Table 1.

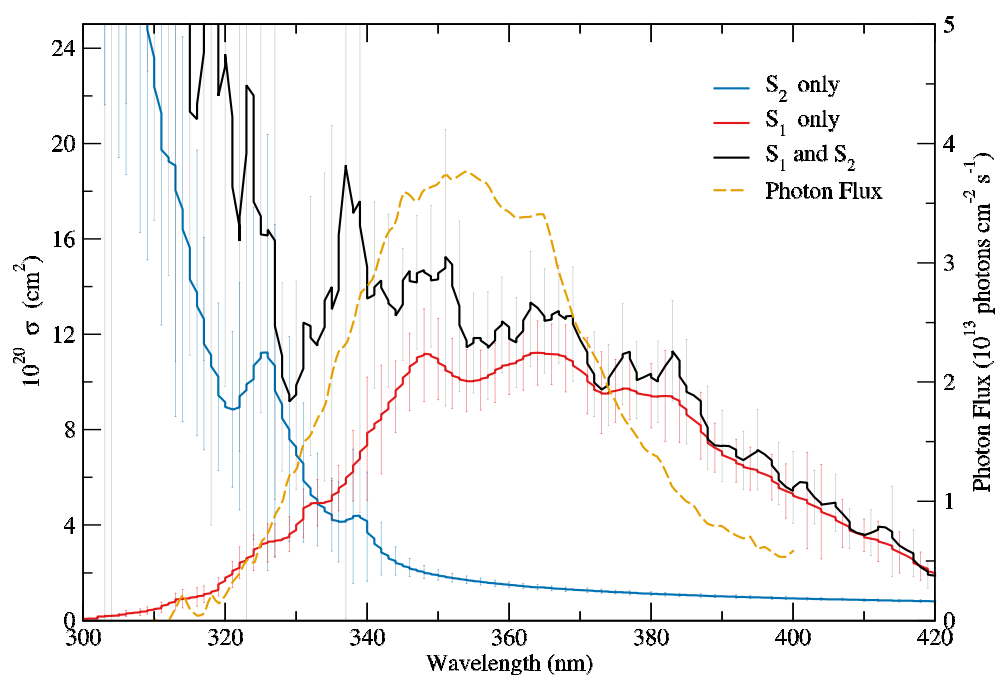


Figure S17 Calculated photoabsorption cross section of C₆-HPALD calculated using the Wigner ensemble method including excitations into the S₁ state only; the S₂ state only; both S₁ and S₂.

The photodissociation rate constant J is then computed by integrating the product of the cross section σ , the incident flux F and quantum yield ϕ (assumed to be 1). Values for the actinic flux are generously provided by John D. Crouse to replicate the experiments in Wolfe *et al.*¹.

$$J = \int_{\lambda_{min}}^{\lambda_{max}} \sigma(\lambda) \phi(\lambda) F(\lambda) d\lambda$$

S5. Optimised geometries at the critical points on the S₁ surface:

S ₁ Transition State			S ₁ /S ₂ MECI				
C	-1.4060189	2.4098252	0.2235875	C	2.88515471	-0.92818978	-0.75884241
C	-1.6798263	1.0453553	-0.4014833	C	1.41203965	-0.59288296	-0.97515944
H	-1.6007691	2.3975766	1.3024825	H	3.42940314	-0.05369480	-0.39234114
H	-2.0497346	3.1755590	-0.2214490	H	3.34760020	-1.24905244	-1.69791842
H	-0.3649798	2.7180209	0.0745596	H	3.01043916	-1.73688608	-0.02837435
H	-2.7220153	0.7451016	-0.2513588	H	1.31457357	0.27216548	-1.63921166

C	-0.8010352	-0.0566923	0.1959860	C	0.66210618	-0.28007680	0.32891398
H	-1.5027929	1.0714333	-1.4846103	H	0.88880100	-1.43181368	-1.45325767
O	-1.1589852	-1.3493592	-0.3627193	O	1.35482785	0.73667542	1.10583675
H	-0.9464474	-0.1069402	1.2850243	H	0.71758141	-1.15563622	0.99648667
C	0.6382591	0.0413216	-0.1641628	C	-0.76116032	0.11248158	0.09942736
C	1.6451761	-0.2963838	0.7070148	C	-1.81437710	-0.72706045	0.33631882
C	3.0178652	-0.2804158	0.3787539	C	-3.16917057	-0.41435878	0.06581716
O	3.5344058	0.0333306	-0.7568154	O	-3.61173010	0.70295957	-0.40744809
H	0.8700502	0.3361463	-1.1848627	H	-0.91383261	1.10531042	-0.31477188
H	1.4044025	-0.6021622	1.7207028	H	-1.63942947	-1.71652301	0.75223380
H	3.7456025	-0.5533040	1.1560210	H	-3.93668791	-1.17476847	0.25961051
O	-2.7049646	-1.6588353	0.1492353	O	1.46384836	2.05283537	0.09424441
H	-2.8058693	-2.4748824	-0.3875351	H	1.82246888	2.64528928	0.79073068

S6. Energies, rotational constants, and frequencies calculated at the critical points.

All of the below values are calculated in Gaussian 16³, with LR-TDDFT/PBE0/6-31G using tight convergence criteria and an ultrafine integration grid.

	S ₁ minimum (B)	S ₁ minimum (C)	TS – S ₁	CI – S ₁ /S ₂ *
Energy (a.u.)	-459.429938897	-459.429169893	-459.42369136	-459.418027248
ZPE correction (a.u)	0.153697	0.153386	0.150686	0.1619025445
Rotational constants	0.06178 0.03267 0.02342	0.07586 0.02710 0.02170	0.07539 0.02689 0.02155	0.0222 0.0251 0.0938
Frequencies	53.7093 69.0555 91.7755 134.5593 145.3678 171.9759 221.3219 225.2273 299.9763 352.2649 387.0304 390.6556 478.609 517.1127 649.0519 709.1161 801.9211 827.045 892.4528 906.2169 943.5918 955.5396 1026.4537 1058.011 1107.599 1180.0393 1184.4502 1214.5041 1291.3523 1311.938 1324.6155 1342.4468 1343.5943 1393.5145 1428.1916 1461.3167 1499.3381 1539.3167	42.3725 68.6738 93.1878 112.3241 147.5971 164.3655 210.9118 233.587 278.9438 300.8378 388.1045 447.713 461.5256 512.0716 660.1531 719.9368 789.8532 829.3933 834.7936 905.0289 944.631 966.1619 1031.0846 1061.9474 1106.8674 1172.6581 1185.0541 1216.4378 1272.7574 1296.4804 1327.2453 1343.5821 1346.6629 1393.9353 1425.6609 1461.0041 1502.7229 1540.7134	-3534.0736 63.7551 67.9529 95.3035 110.0446 148.6376 207.6926 228.0155 253.1427 275.4055 308.6733 364.2645 434.6985 456.206 497.9537 680.2171 791.6283 826.7497 865.5645 905.0682 956.5599 959.6579 1025.5298 1071.0154 1085.7322 1110.114 1132.9102 1162.4788 1213.9031 1274.7914 1292.0703 1315.029 1337.7966 1345.5383 1379.918 1414.6639 1461.0081 1539.1839	68.62 78.221 84.668 128.213 181.793 223.116 253.395 254.783 301.067 329.293 362.679 410.98 485.264 583.909 698.771 771.322 793.207 872.964 915.326 960.249 1036.699 1058.41 1087.157 1093.907 1137.154 1163.242 1185.308 1262.67 1287.216 1310.993 1338.057 1352.212 1376.988 1398.868 1455.576 1521.33 1539.105 1549.307

1543.0902	1543.8922	1542.1446	1603.235
1550.8704	1550.9794	1549.4011	3018.911
1598.7604	1609.256	1604.491	3067.174
3066.7762	3062.8107	3049.8769	3067.697
3075.598	3064.5537	3050.92	3070.362
3079.3257	3072.6858	3063.5567	3134.348
3091.1291	3075.6386	3078.6837	3153.494
3129.6292	3129.3525	3134.677	3177.919
3156.2406	3152.4157	3154.9103	3209.011
3162.2071	3158.2418	3159.2982	3235.128
3211.1928	3222.2468	3218.3714	3644.865
3237.3168	3238.926	3232.116	
3623.5612	3650.8246	3646.0593	

S7. Branching space at the MECI

Gradient difference (g)				Derivative coupling (ETF corrected) (h)			
C	0.102056E-03	-0.621470E-04	-0.390281E-03	C	-4.484668	-4.838438	18.284332
C	0.297746E-03	0.211320E-03	0.118439E-02	C	-12.150318	39.701432	-69.764144
H	-0.429340E-04	0.161000E-04	0.514220E-04	H	3.540401	0.003348	-4.296759
H	0.156898E-03	-0.630570E-04	0.194940E-04	H	-7.843623	3.484781	1.387522
H	-0.128200E-04	0.749900E-05	0.466640E-04	H	-0.890071	0.491148	-2.669058
H	-0.926970E-04	-0.730590E-04	-0.737730E-04	H	7.949269	5.579241	-2.076216
C	-0.271767E-02	-0.617192E-03	-0.439607E-02	C	191.653690	-145.164158	287.966800
H	0.179710E-04	0.226490E-04	-0.988220E-04	H	-2.392614	-3.880188	9.528667
O	0.384463E-02	0.137730E-01	-0.155984E-01	O	-240.341234	-1192.585893	767.883422
H	0.546384E-03	0.515009E-03	0.576439E-03	H	-60.385774	-51.681452	-68.595717
C	0.349772E-02	0.206840E-02	-0.369046E-03	C	-279.340661	-176.445168	48.087380
C	-0.842186E-02	-0.983095E-03	-0.356232E-03	C	643.550588	81.899861	34.330309
C	0.106874E-01	-0.965713E-02	0.992957E-02	C	-841.867843	916.299623	-461.119380
O	-0.497100E-02	0.736638E-02	-0.693473E-02	O	389.370823	-688.428675	313.400606
H	0.553938E-03	-0.484603E-03	-0.168809E-03	H	-33.073840	18.498041	-1.989105
H	-0.623553E-03	-0.216590E-04	-0.326236E-03	H	47.733292	-4.781142	15.271671
H	-0.874117E-03	0.883858E-03	-0.855460E-03	H	68.546600	-81.100604	38.675828
O	-0.165508E-02	-0.128428E-01	0.176537E-01	O	107.048607	1265.057512	-913.533304
H	-0.293047E-03	-0.595600E-04	0.106157E-03	H	23.377372	17.890744	-10.772851

The derivative coupling vector **h** was calculated at the MECI, (TDDFT/PBE0/6-31G), in Q-Chem, following the procedure described in Ou *et al.*¹¹

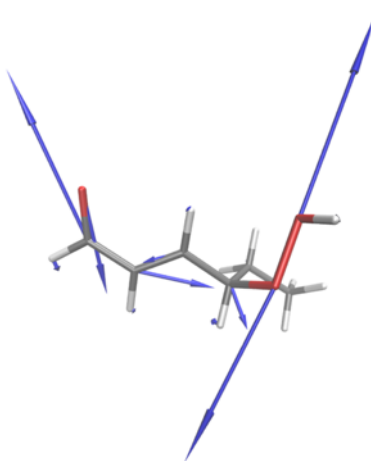


Figure S18 Derivative coupling vector at the S₁/S₂ MECI

S8. Peroxide bond length coordinate R(O-O) throughout the NAMD simulation.

Figure S6 illustrates that for most cases trajectories that cross the 1.75 Å threshold will dissociate soon after. The average -O-OH bond length stays close to 1.5 Å throughout.

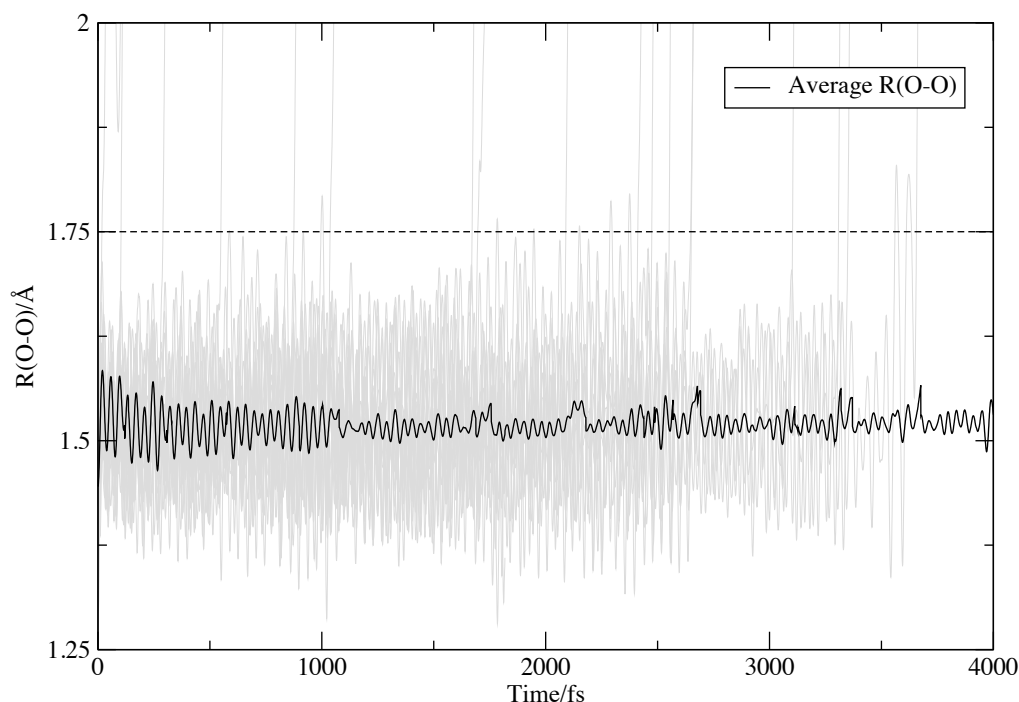


Figure S19 Peroxide bond length for each of 50 trajectories (initiated at the conformer B geometry) showing that crossing mostly occurred once the trajectory surpassed the 1.75 Å threshold.

S9. Testing timestep sensitivity of FSSH

Running FSSH requires a judicious choice of many parameters, one of which is the time step (dt) with which the classical degrees of freedom evolve on the PESs. In most cases, this decision is made by selecting the smallest dt for a given computational cost, to maximise the accuracy of the dynamics. However, what exactly is compromised when dt is too large?

For example, the accuracy of the classical integration of nuclear coordinates may be diminished. The more subtle point is that the transition probabilities between states also depend on time discretization¹². At each time step the time derivative coupling (TDC) is calculated to determine if a hop to another adiabatic state occurs and when TDC is very localised it can be poorly resolved or missed altogether.

Meek et al. highlighted this problem for trivially unavoided crossings (TUC)¹³ which are $(3N-7)$ dimensional intersections between two weakly coupled states, where N is the number of nuclear degrees of freedom. If the coupling between the states is infinitesimal, a crossing trajectory must necessarily remain on the same diabatic state. As it passes through the seam there would be a sudden narrow spike in the TDC which might not be resolved with a larger dt , and so the trajectory will, incorrectly, move to a different diabatic state. For $(3N-8)$ dimensional conical intersections this problem is less significant, as the nonadiabatic coupling is highly localised in position space.

In this case, the topology of the C_6 -HPALD seam can be described as a TUC as there is an effective $(3N-7)$ crossing at the intersection of the $n\pi^*$ and $n'\sigma^*$ diabatic states with a weak nonadiabatic coupling between them. Slowness of the dissociation process limits us in how small the time step can

be, but it becomes necessary to verify the extent to which this might affect the outcomes of the FSSH dynamics.

Although the loss of OH typically takes picoseconds, many trajectories encounter the (3N-7) seam in the first 50 fs of the simulation. It is then possible to explore how the shape of the TDC is affected by the timestep and to see if the spike in TDC is too sharp to detect with $dt=0.5$ fs. Three example trajectories were taken from the set initiated at conformer C and repeated for 50 fs using identical initial conditions for $dt = 0.25$; $dt = 0.1$ fs; $dt = 0.05$ fs; $dt = 0.025$ fs. Results are shown in Figure S20.

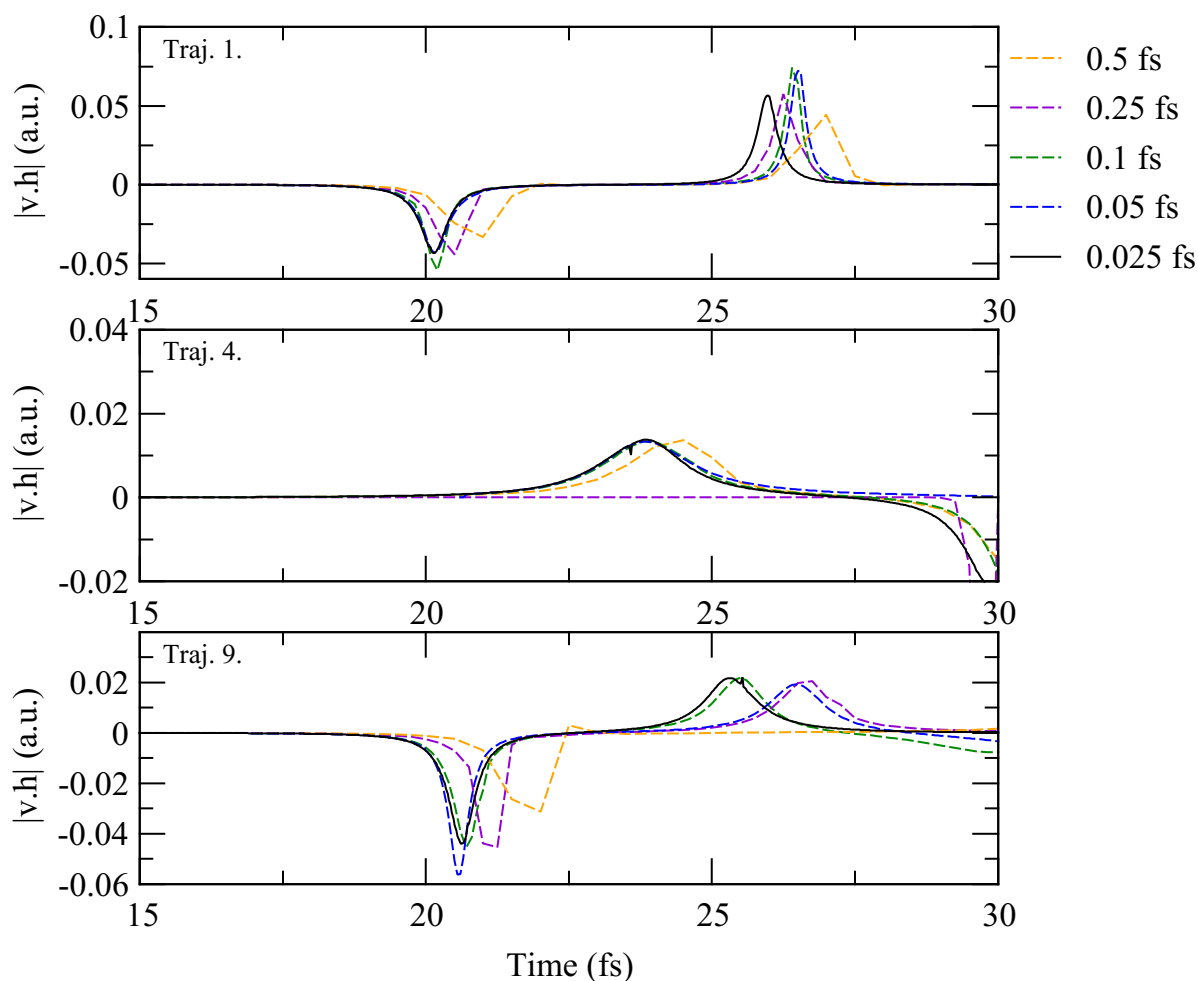


Figure S20 Convergence of time derivative coupling with time step size for three example trajectories in the first 30 fs of the simulation.

Here we see the results converging with progressively smaller values of dt . Ideally, the trajectories should be run with at least a 0.1 fs timestep to properly capture the shape of the TDC, however the computational cost of doing this is prohibitive. The peaks are still present for 0.5 fs time step trajectories, even though they are visibly coarser.

Most trajectories encounter this seam multiple times, so it is still possible that the error in the shape of the TDC peak for 0.5 fs time step may affect the long-time dynamics of OH loss in HPALD. Full length trajectories were run to look for trends in dissociation behaviour between $dt = 0.25$ fs and $dt = 0.5$ fs. For each of a set of 3 IC, we ran 20 replicas which were seeded with a different random number. Results can be seen in Figure S21. These results appear to indicate that the time step size makes no clear difference to the rate of OH loss and so on this basis we conclude that it is safe to use a 0.5 fs time step for FSSH dynamics.

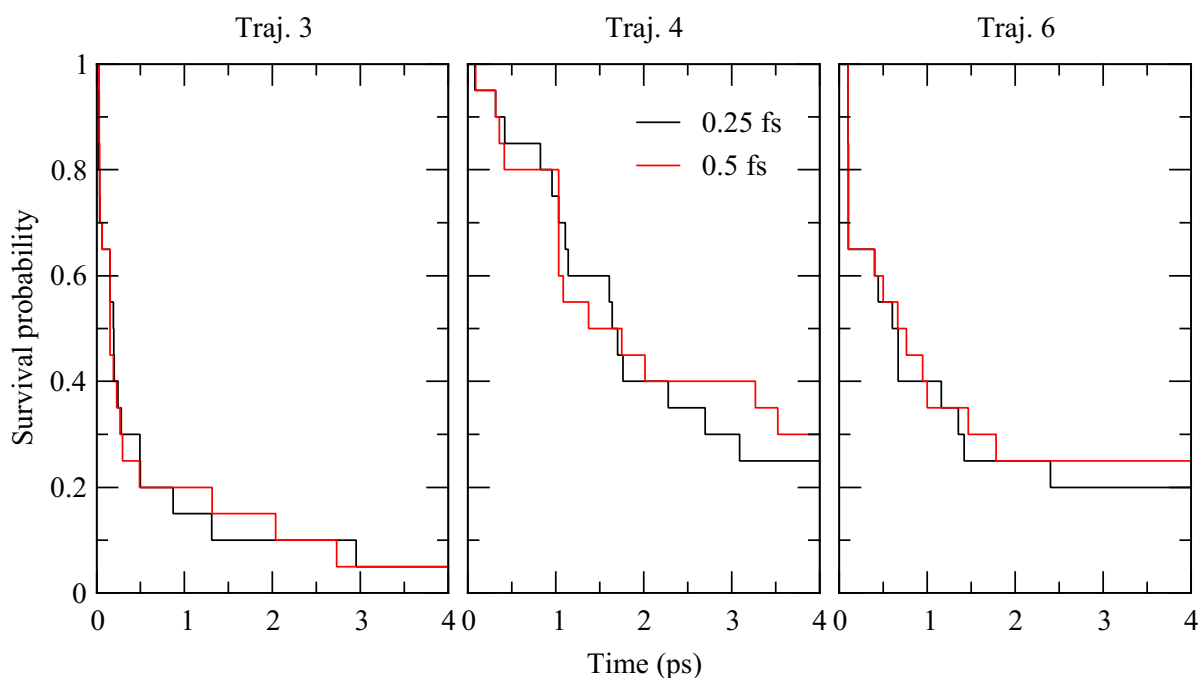


Figure S21 Impact of time step size on the rate of OH loss in HPALD.

S10. Parameters of the diabatic states fitted to the adiabatic surface scan across the eigenvector coordinate (with LR-TDDFT/PBE0)

Implementation of the Zhu-Nakamura equation in MESMER requires an analytic form of the diabatic crossing. These equations were fitted to the

Bound diabatic potential $E_{\pi^*}(R)$ fitted to a harmonic function

$$E_{\pi^*}(R) = A_{\pi^*} \times (R - \beta_{\pi^*})^2 + \varepsilon_{\pi^*}$$

Dissociative diabatic potential $E_{\sigma^*}(R)$ fitted to an exponential decay

$$E_{\sigma^*}(R) = A_{\sigma^*} \times e^{-R \times \beta_{\sigma^*}} + \varepsilon_{\sigma^*}$$

Parameter fitting was performed in Gnuplot v5.2 with resulting parameters are listed in the following table:

Parameter	Value	Standard Error
A_{σ^*}	495.051	± 15.01
β_{σ^*}	-0.119809	± 0.00349
ε_{σ^*}	11.0345	± 0.1939
A_{π^*}	66.9186	± 2.388
β_{π^*}	3.76346	± 1.307
ε_{π^*}	-46.4714	± 2.382
H_{12}	3.00481	± 0.01141

S11. Sensitivity testing the EGME model

Some parameters included in the EGME calculation might have a significant impact on the result. We test the robustness of the EGME model by comparing the result when those parameters are varied.

An assumption we make in the EGME model is that it is valid to use the average initial energy from TSH initial conditions, rather than a distribution. Figure S9 shows results of an EGME model built to replicate the original 10 trajectories starting from the minimum of conformer C. A ZN-EGME calculation is performed for each trajectory IC illustrating that the model is robust to modest variation in initial energy.

EGME results can also be sensitive to frequencies, especially low frequencies that have a significant impact on the density of states. Figure S9 compares EGME results calculated using critical points optimised with tight convergence conditions and a fine integration grid against results calculated with a standard grid and convergence criteria. Even with a slight difference in frequencies the decay curves are visibly different. This highlights the importance of using frequencies calculated in a consistent way for each isomer when constructing an EGME model.

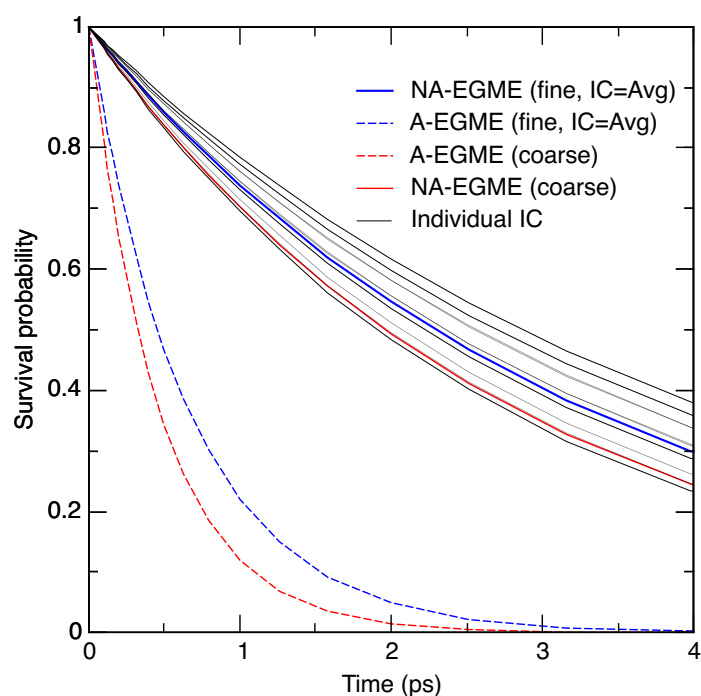


Figure S22 Result of EGME calculation intended to replicate the dissociation of the first 10 trajectories of conformer C.

S12. Parameters of the diabatic states fitted to the adiabatic surface scan across the eigenvector coordinate (with MS(5)-CASPT2(10,8)/6-31G*)

Table S3 Fitted parameters for the diabatic potentials around the TS calculated with CASPT2.

Parameter	Value	Standard Error
A_{σ^*}	835.318	± 73.88
β_{σ^*}	-0.113482	± 0.009752
ϵ_{σ^*}	9.51291	± 0.8865
A_{π^*}	50.3379	± 4.159
β_{π^*}	5.85351	± 0.4645
ϵ_{π^*}	-29.9859	± 4.144
H_{12}	0.823152	± 0.04453

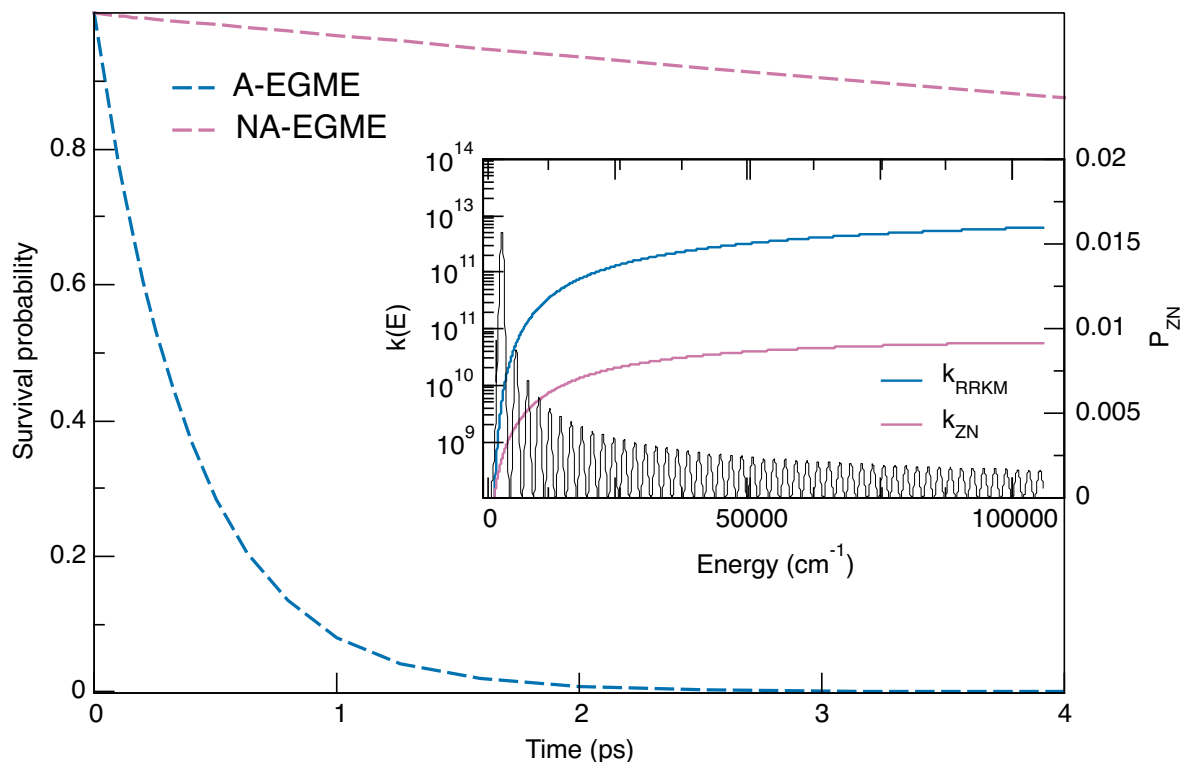


Figure S23 Results of EGME calculations based on MS-CASPT2(10,8) energies at the critical points. Inset contains the microcanonical rate coefficients calculated for each energy grain from RRKM (GS-EGME) and ZN (NA-EGME).

S13. NA-EGME results with hindered rotor corrections.

Results obtained by re-running the EGME calculations with the hindered rotor vibrations projected out of the Hessian. Using $S_1(B)$ minimum and TS, both optimised with tight convergence criteria and ultrafine integration grid.

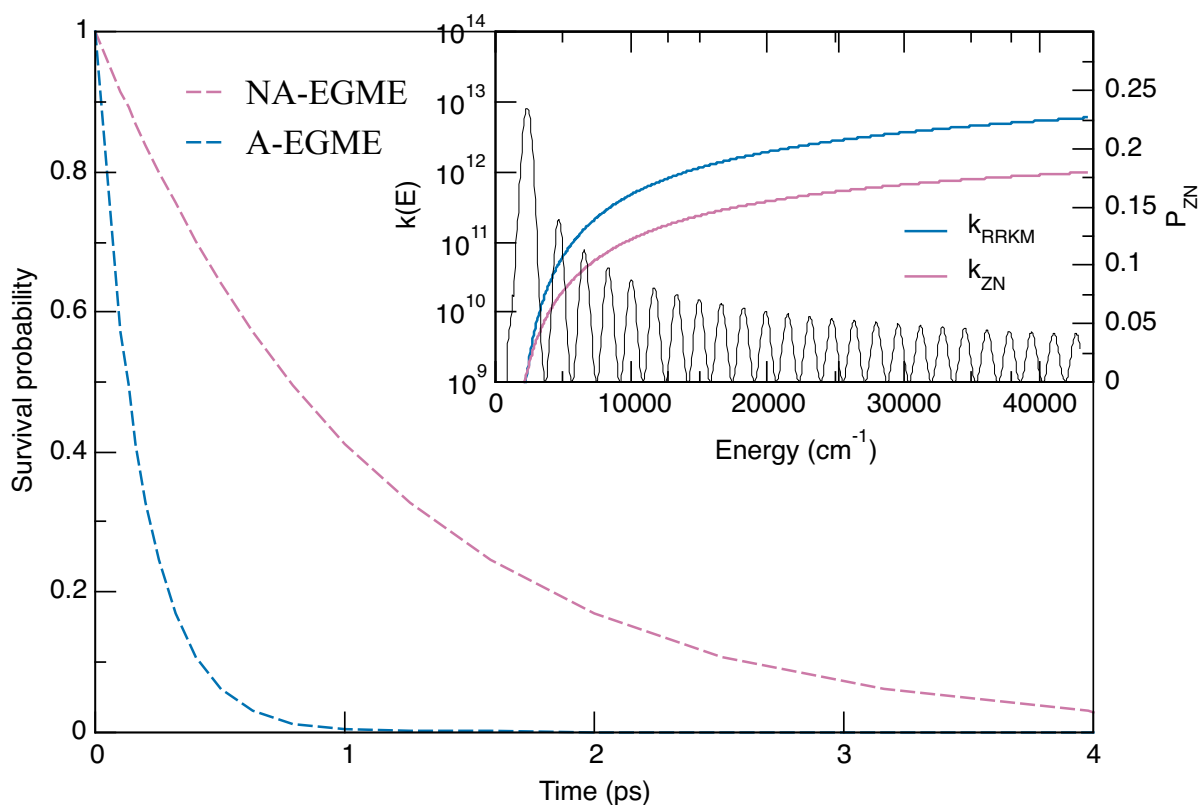


Figure S24 EGME results with hindered rotor corrections.

S15. Zhu-Nakamura equations

This section contains the full set of Zhu-Nakamura equations, as implemented in MESMER¹⁴.

Figure S25 is an example schematic of a nonadiabatic tunnelling (NT) type crossing, defined by the opposing slopes of the two crossing diabats. This is in contrast to a Landau Zener type crossing for which there is a similar set of equations, references where they can be found which are available. The figure highlights the features of the crossing that will be used in the following equations, both in the adiabatic (black) and diabatic (red) representations.

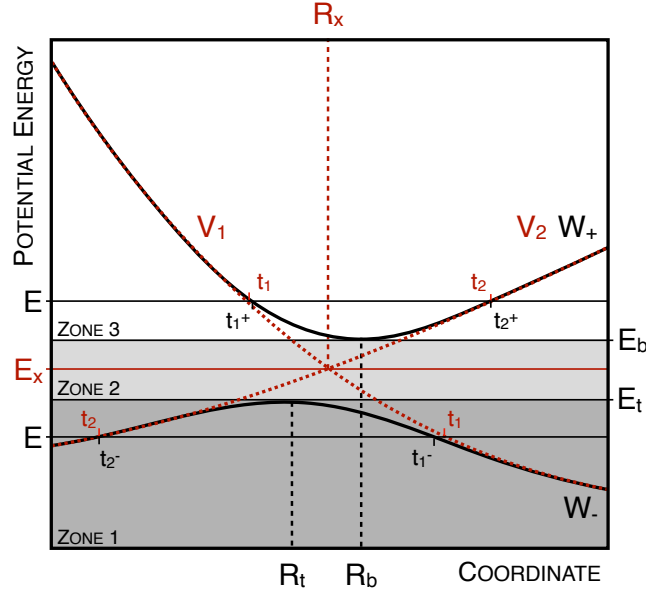


Figure S25: NT type crossing. Red, black features correspond to diabatic, adiabatic representations respectively.

Variable naming in the following equations will follow the conventions of the original paper. To improve comprehension of more cumbersome equations, dummy variables will be also be used and will be labelled g_n .

In the diabatic representation we define parameters a^2 and b^2 as

$$a^2 = \frac{\hbar^2 F(F_1 - F_2)}{16\mu V_x^3}$$

$$b^2 = (E - E_x) \times \frac{(F_1 - F_2)}{2FV_x}$$

where F_n is the slope of the diabatic potential, $F = \sqrt{F_1 F_2}$, reduced mass of the system is μ and V_x is the inter-state coupling. The crossing is split into 3 different energy ranges (zones – shown in Figure S25) which require separate sets of equations. In MESMER, the algorithm will solve for the Zhu-Nakamura transition probability P_{12} at each energy grain.

Zone 1: $E \leq E_t$

We begin by calculating the integral of the tunnelling action δ through a single potential barrier on the adiabatic surface W_-

$$K_-(R) = \frac{1}{\hbar} \sqrt{2\mu(E - W_-(R))}$$

$$\delta = \int_{t_2^-}^{t_1^-} |K_-(R)| dR$$

Next, we need adiabatic parameter σ which captures the effect of nonadiabatic transition between the two adiabatic surfaces. $\Gamma(X)$ is the standard Gamma function.

$$\sigma = \frac{\pi}{2a|b|} \frac{\left(6 + 10\sqrt{1 - \frac{1}{b^4}}\right)^{\frac{1}{2}}}{1 + \sqrt{1 - \frac{1}{b^4}}}$$

$$\sigma_c = \sigma \left(1 - 0.32 \times 10^{-\frac{2}{a^2}} e^{-\delta} \right)$$

$$B(X) = \frac{2\pi X^{2X} e^{-2X}}{X\Gamma^2(X)}$$

Broadly, $e^{-2\delta}$ can be interpreted as a Gamow factor for tunnelling and $B(\sigma_c/\pi)$ as the impact of nonadiabatic coupling on the tunnelling. Combining these factor yields the expression for the transition probability for energies $\leq E_t$

$$P_{12} = \frac{B(\sigma_c/\pi)e^{-2\delta}}{\left(\left(1 + \frac{a}{2(1+a)} B(\sigma_c/\pi)e^{-2\delta} \right)^2 + B(\sigma_c/\pi)e^{-2\delta} \right)}$$

Zone 2: $E_t \leq E \leq E_b$

We begin by defining two empirical corrections g_1 and g_2 that ensure the full range of coupling strengths is covered. W is a factor of the Stokes constant.

$$g_1 = \frac{a - 3b^2}{a + 3} \sqrt{1.23 + b^2}$$

$$g_2 = 0.38 \frac{(1 + b^2)^{1.2 - 0.4b^2}}{a^2}$$

$$W = \int_0^\infty \frac{1 + g_2}{a^{2/3}} \cos \left(\frac{t^3}{3} - \frac{b^2 t}{a^{2/3}} - \frac{g_1 t}{a^{2/3} (0.61\sqrt{2 + b^2} + a^{1/3}t)} \right) dt$$

Combining these factors gives us the transition probability.

$$P_{12} = \frac{W^2}{1 + W^2}$$

Zone 3: $E \leq E_b$

Integral of the classical action on the upper adiabatic surface σ and nonadiabatic transition parameter δ are used to calculate the phase ϕ

$$K_+(R) = \frac{1}{\hbar} \sqrt{2\mu(E - W_+(R))}$$

$$\sigma = \int_{t_1^+}^{t_2^+} |K_+(R)| dR$$

$$\delta = \frac{\pi}{16ab} \frac{(6 + 10\sqrt{1 - 1/b^4})^{1/2}}{1 + \sqrt{1 - 1/b^4}}$$

$$\phi = \sigma + \frac{\delta}{\pi} - \frac{\delta}{\pi} \ln \left(\frac{\delta}{\pi} \right) + \frac{\pi}{4} - g_3 + \text{Arg} \Gamma \left(i \frac{\delta}{\pi} \right)$$

where g_3 is

$$g_3 = \frac{0.23a^{1/2}}{a^{1/2} + 0.75} 40^{-\sigma}$$

Finally, we use the Landau-Zener transition probability p

$$p = \exp \left(\frac{-\pi}{4a} \sqrt{\frac{2}{b^2 + (b^4 + g_4)^{1/2}}} \right)$$

where g_4 is

$$g_4 = -0.72 + 0.62a^{1.43}$$

to yield the final expression for the nonadiabatic transition probability in zone 3.

$$P_{12} = \frac{4\cos^2\phi}{4\cos^2\phi + p^2/(1-p)}$$

S16. MESMER input files for:

- a) RRKM calculation of seam crossing rate – in file *rrkm.xml*
- b) ZN calculation of seam crossing rate – in file *zn.xml*

Bibliography

1. Wolfe, G. D.; Crouse, J. D.; Parrish, J. D.; St. Clair, J. M.; Beaver, M. R.; Paulot, F.; Yoon, T. P.; Wennberg, P. O.; Keutsch, F. N., Photolysis, OH reactivity and ozone reactivity of a proxy for isoprene-derived hydroperoxyenals (HPALDs). *Phys. Chem. Chem. Phys.* **2012**, *14*, 7276-7286.
2. *Avogadro: an open-source molecular builder and visualization tool.*, 1.2.0; <http://avogadro.cc/>.
3. Frisch, M. J.; Trucks, G. W.; Schlegel, H. B.; Scuseria, G. E.; Robb, M. A.; Cheeseman, J. R.; Scalmani, G.; Barone, V.; Petersson, G. A.; Nakatsuji, H.; Li, X.; Caricato, M.; Marenich, A. V.; Bloino, J.; Janesko, B. G.; Gomperts, R.; Mennucci, B.; Hratchian, H. P.; Ortiz, J. V.; Izmaylov, A. F.; Sonnenberg, J. L.; Williams-Young, D.; Ding, F.; Lipparini, F.; Egidi, F.; Goings, J.; Peng, B.; Petrone, A.; Henderson, T.; Ranasinghe, D.; Zakrzewski, V. G.; Gao, J.; Rega, N.; Zheng, G.; Liang, W.; Hada, M.; Ehara, M.; Toyota, K.; Fukuda, R.; Hasegawa, J.; Ishida, M.; Nakajima, T.; Honda, Y.; Kitao, O.; Nakai, H.; Vreven, T.; Throssell, K.; Montgomery, J. A., Jr.; Peralta, J. E.; Ogliaro, F.; Bearpark, M. J.; Heyd, J. J.; Brothers, E. N.; Kudin, K. N.; Staroverov, V. N.; Keith, T. A.; Kobayashi, R.; Normand, J.; Raghavachari, K.; Rendell, A. P.; Burant, J. C.; Iyengar, S. S.; Tomasi, J.; Cossi, M.; Millam, J. M.; Klene, M.; Adamo, C.; Cammi, R.; Ochterski, J. W.; Martin, R. L.; Morokuma, K.; Farkas, O.; Foresman, J. B.; Fox, D. J. *Gaussian 16, Revision C.01*, Gaussian, Inc.: Wallingford CT, 2016.
4. Peeters, J.; Nguyen, T. L.; Vereecken, L., HOx radical regeneration in the oxidation of isoprene. *Phys. Chem. Chem. Phys.* **2009**, *11* (28), 5935-9.
5. Tozer, D. J., Relationship between long-range charge-transfer excitation energy error and integer discontinuity in Kohn–Sham theory. *J. Chem. Phys.* **2003**, *119* (12697).
6. Levine, B. G.; Ko, C.; Quenneville, J.; Martinez, T. J., Conical intersections and double excitations in time-dependent density functional theory. *Mol. Phys.* **2006**, *104* (5-7).
7. *TURBOMOLE*, V7.1; a development of University of Karlsruhe and Forschungszentrum Karlsruhe GmbH, 1989-2007, TURBOMOLE GmbH, since 2007; available from <http://www.turbomole.com>.: 2017.
8. Werner, H.-J.; Knowles, P. J.; Knizia, G.; Manby, F. R.; Schütz, M.; Celani, P.; Györfly, W.; Kats, D.; Korona, T.; Lindh, R.; Mitrushenkov, A.; Rauhut, G.; Shamasundar, K. R.; Adler, T. B.; Amos, R. D.; Bennie, S. J.; Bernhardsson, A.; Berning, A.; Cooper, D. L.; Deegan, M. J. O.; Dobbyn, A. J.; Eckert, F.; Goll, E.; Hampel, C.; Hesselmann, A.; Hetzer, G.; Hrenar, T.; Jansen, G.; Köppl, C.; Lee, S. J. R.; Liu, Y.; Lloyd, A. W.; Ma, Q.; Mata, R. A.; May, A. J.; McNicholas, S. J.; Meyer, W.; III, T. F. M.; Mura, M. E.; Nicklass, A.; O'Neill, D. P.; Palmieri, P.; Peng, D.; Pflüger, K.; Pitzer, R.; Reiher, M.; Shiozaki, T.; Stoll, H.; Stone, A. J.; Tarroni, R.; Thorsteinsson, T.; Wang, M.; Welborn, M. *MOLPRO, version 2019.2, a package of ab initio programs*, 2019.
9. Galván, I. F.; Vacher, M.; Alavi, A.; Angeli, C.; Aquilante, F.; Autschbach, J.; Bao, J. J.; Bokarev, S. I.; Bogdanov, N. A.; Carlson, R. K.; Chibotaru, L. F.; Creutzberg, J.; Dattani, N.;

- Delcey, M. G.; Dong, S. S.; Dreuw, A.; Freitag, L.; Frutos, L. M.; Gagliardi, L.; Gendron, F.; Giussani, A.; González, L.; Grell, G.; Guo, M.; Hoyer, C. E.; Johansson, M.; Keller, S.; Knecht, S.; Kovačević, G.; Källman, E.; Manni, G. L.; Lundberg, M.; Ma, Y.; Mai, S.; Malhado, J. P.; Malmqvist, P. Å.; Marquetand, P.; Mewes, S. A.; Norell, J.; Olivucci, M.; Oppel, M.; Phung, Q. M.; Pierloot, K.; Plasser, F.; Reiher, M.; Sand, A. M.; Schapiro, I.; Sharma, P.; Stein, C. J.; Sørensen, L. K.; Truhlar, D. G.; Ugandi, M.; Ungur, L.; Valentini, A.; Vancoillie, S.; Veryazov, V.; Weser, O.; Wesolowski, T. A.; Widmark, P.-O.; Wouters, S.; Zech, A.; Zobel, J. P.; Lindh, R., OpenMolcas: From Source Code to Insight. *J. Chem. Theory Comput.* **2019**, *15* (11), 5925-5964.
10. Crespo-Otero, R.; Barbatti, M., Spectrum simulation and decomposition with nuclear ensemble: Formal derivation and application to benzene, furan and 2-phenylfuran. *Theo. Chem. Acc.* **2012**, *131* (6), 1-14.
11. Ou, Q.; Bellchambers, G. D.; Furche, F.; Subotnik, J. E., First-order derivative couplings between excited states from adiabatic TDDFT response theory. *J. Chem. Phys.* **2015**, *142* (064114).
12. Parker, S. M.; Schiltz, C. J., Surface hopping with cumulative probabilities: Even sampling and improved reproducibility. *J. Chem. Phys.* **2020**, *153* (17).
13. Meek, G. A.; Levine, B. G., Accurate and efficient evaluation of transition probabilities at unavoided crossings in ab initio multiple spawning. *Chem. Phys.* **2015**, *460*, 117-124.
14. (a) Glowacki, D. R.; Liang, C.-H.; Morley, C.; Pilling, M. J.; Robertson, S. H., MESMER: an open-source master equation solver for multi-energy well reactions. *J. Phys. Chem. A* **2012**, *116*, 9545-9560; (b) Robertson, S. H.; Glowacki, D. R.; Liang, C.-H.; Morley, C.; Shannon, R.; Blitz, M.; Pilling, M. J. *MESMER v6.0 (master equation solver for multi energy well reactions)*, 2020.